

Experimental studies of the NaCs $12(0^+)$ [$7^1\Sigma^+$] state: Spin-orbit and non-adiabatic interactions and quantum interference in the $12(0^+)$ [$7^1\Sigma^+$] and $11(0^+)$ [$5^3\Pi_0$] emission spectra

C. Faust,^{1,a)} J. Jones,^{1,b)} J. Huennekens,¹ and R. W. Field²

¹Department of Physics, Lehigh University, 16 Memorial Drive East, Bethlehem, Pennsylvania 18015, USA

²Department of Chemistry, Massachusetts Institute of Technology, Cambridge, Massachusetts 02139, USA

(Received 16 December 2016; accepted 31 January 2017; published online 9 March 2017)

We present results from experimental studies of the $11(0^+)$ and $12(0^+)$ electronic states of the NaCs molecule. An optical-optical double resonance method is used to obtain Doppler-free excitation spectra. Selected data from the $11(0^+)$ and $12(0^+)$ high-lying electronic states are used to obtain Rydberg-Klein-Rees and Inverse Perturbation Approach potential energy curves. Interactions between these two electronic states are evident in the patterns observed in the bound-bound and bound-free fluorescence spectra. A model, based on two separate interaction mechanisms, is presented to describe how the wavefunctions of the two states mix. The electronic parts of the wavefunctions interact via spin-orbit coupling, while the individual rotation-vibration levels interact via a second mechanism, which is likely to be non-adiabatic coupling. A modified version of the BCONT program was used to simulate resolved fluorescence from both upper states. Parameters of the model that describe the two interaction mechanisms were varied until simulations were able to adequately reproduce experimental spectra. *Published by AIP Publishing.* [<http://dx.doi.org/10.1063/1.4976630>]

I. INTRODUCTION

A striking feature of atomic and molecular spectroscopy is that quantum interference effects are often evident when more than one quantum mechanical pathway leads to the same final state.^{1–7} Interference effects form the basis of many interesting phenomena including most quantum control schemes.^{8–18} For example, it has been demonstrated in Li_2 that the spin-orbit interaction between two neighboring levels that belong to different electronic states, but with the same rotational quantum number, J , can be enhanced by shifting one of the levels closer into resonance with the other using the Autler-Townes (AC Stark) effect.^{19,20} In a related experiment, the collisional excitation transfer rate between two electronic states was also enhanced using the Autler-Townes effect.²¹ Constructive and destructive interference between singlet and triplet pathways, leading, in some cases, to complete disappearance of spectral lines, was observed in experiments on the NaK molecule.²²

Alkali diatomic molecules are also central to current efforts to produce ultracold molecules in their lowest ro-vibrational levels.^{23–37} Heteronuclear alkali diatomic molecules are of particular interest since each molecule has a permanent electric dipole moment, which can, in principle, be oriented in an optical trap or optical lattice. Because of this feature, the heteronuclear alkali molecules have been suggested as candidates for qubits in quantum computing schemes.^{38–41}

The NaCs molecule has the second largest permanent electric dipole moment of all heteronuclear alkali diatomic molecules, and it is therefore of considerable interest for various ultracold molecule applications.^{35,36,42–47}

Due to this interest, a number of spectroscopic investigations of NaCs have been carried out in recent years. NaCs was first studied at high resolution by Onomichi and Katō⁴⁸ and by Diemer *et al.*⁴⁹ Docenko *et al.*^{44,50} accurately mapped the NaCs ground state, and a detailed study by Zaharova *et al.*⁵¹ sorted out the important $b^3\Pi \sim A^1\Sigma^+$ spin-orbit perturbed manifold, the levels of which serve as intermediate states in the double-resonance experiments described below and in the work of Ashman *et al.*⁵² Docenko *et al.*⁵³ used high-resolution Fourier-transform spectroscopy to fit the potential of the $(3)^1\Pi$ state and Grochola *et al.*⁴⁶ mapped the $c^3\Sigma^+(\Omega = 1)$ state using polarization labeling, photoassociation, and pulsed laser depletion spectroscopies. In our lab, Ashman *et al.*⁵² determined Dunham coefficients for the $5^3\Pi_0^+$ state and mapped the potential energy curve using the inverted perturbation approach (IPA). Analysis of resolved $5^3\Pi_0^+ \rightarrow 1(a)^3\Sigma^+$ bound-free fluorescence spectra was used to map the repulsive wall of the $1(a)^3\Sigma^+$ state and to determine the $5^3\Pi_0^+ \rightarrow 1(a)^3\Sigma^+$ relative transition dipole moment function. The current work was also aided immensely by recent theoretical work. Non-relativistic NaCs potential energy curves were calculated by Korek *et al.*,⁵⁴ while more recently Korek, Bleik, and Allouche⁵⁵ published relativistic curves (including spin-orbit interactions). Aymar and Dulieu⁵⁶ calculated theoretical transition dipole moment functions and their $5^3\Pi_0^+ \rightarrow 1(a)^3\Sigma^+$ dipole moment function was found to be in good agreement with experiment in Ref. 52.

This paper describes experimental studies of the NaCs $11(0^+)$ and $12(0^+)$ electronic states. In this work, we have used

^{a)}Present Address: Physics Department, Susquehanna University, 514 University Avenue, Selinsgrove, Pennsylvania 17870, USA.

^{b)}Present Address: Department of Physics and Astronomy, Colgate University, Ho Science Center, 13 Oak Drive, Hamilton, New York 13346, USA.

optical-optical double resonance (OODR) laser spectroscopy to measure energies of 214 ro-vibrational levels of the NaCs $12(0^+)$ state [$7^1\Sigma^+$ in Hund's case (*a*) notation] and mapped out the $12(0^+)$ potential energy curve using the Rydberg-Klein-Rees (RKR) and IPA methods. The NaCs Hund's case (*a*) electronic states $5^3\Pi_{0^+}$ and $7^1\Sigma^+$ interact via spin-orbit interaction to produce the Hund's case (*c*) states $11(0^+)$ and $12(0^+)$. However, we have found that individual pairs of ro-vibrational levels of the $11(0^+)$ and $12(0^+)$ states appear to interact through a second mechanism, which we believe is non-adiabatic coupling. Quantum interference in our model of these interactions creates interesting mixed state wavefunctions that result in unusual intensity distributions in resolved $11(0^+)$, $12(0^+) \rightarrow 1(X)^1\Sigma^+$, $1(a)^3\Sigma^+$ fluorescence. We have carried out quantum mechanical simulations of the bound-bound and bound-free emission spectra to demonstrate the plausibility of our two-mechanisms' argument.

This paper is organized as follows. In Sec. II, we describe the experimental setup and the experimental techniques used. Section III reports our analysis and results for the NaCs $12(0^+)$ [$7^1\Sigma^+$] electronic state, including a mapping of the lower part of the $12(0^+)$ potential energy curve. Section IV discusses the interactions between the NaCs $11(0^+)$ and $12(0^+)$ electronic states and our model of the interactions between these states. We also demonstrate how these interactions affect the mixed state wavefunctions that result in the unusual bound-free fluorescence patterns similar to those we observe. Our conclusions appear in Sec. V.

II. THE EXPERIMENT

The experimental setup is very similar to that used in Ref. 52 and is shown schematically in Fig. 1. The experiment is centered around a six arm heat pipe oven containing sodium and cesium metal. The central region of the oven was heated to temperatures in the range 290-310 °C using clamshell heaters controlled by Variacs. To prevent the alkali metal from coming into contact with the windows, argon buffer

gas flowed into the oven through inlets near the windows and the region of each arm near the window was maintained at approximately room temperature with external water cooling coils.

Heating the alkali metals produces atomic Na and Cs vapor and the molecular species Na_2 , Cs_2 , and NaCs. Valves regulating the flow of buffer gas from the tank and the vacuum system pumping speed were adjusted such that the pressure in the oven was $\sim 3\text{--}5$ Torr.

To investigate high-lying electronic states of NaCs, we employed an Optical-Optical Double Resonance (OODR) technique. The OODR method, using narrowband continuous wave (cw) lasers, is inherently Doppler free. In the present experiment, we employed two single-mode, tunable Ti:Sapphire and dye lasers (see Fig. 1) in a pump-probe scheme.

The pump laser is a Coherent 899-29 Titanium:Sapphire (Ti:Sapphire) cw ring laser, which is pumped by all visible lines of a Coherent Innova 200 argon ion laser. 10 W of pump power produces 100–500 mW from the Ti:Sapphire laser, which allows a wavelength tuning range of 780–900 nm. We scanned the frequency of the pump (Ti:Sapphire) laser while monitoring the anode current from a freestanding Hamamatsu R406 photomultiplier tube (“Total Red PMT” in Fig. 1). Once a particular pump transition [$1(b)^3\Pi(v_b, J) \sim 2(A)^1\Sigma^+(v_A, J) \leftarrow 1(X)^1\Sigma^+(v_X, J \pm 1)$] was identified and properly assigned, the pump laser frequency was fixed to the peak of this transition. Due to spin-orbit interactions, the pumped level of the intermediate [$b^3\Pi \sim A^1\Sigma^+$] state has both singlet and triplet characters.

The probe laser is a Coherent 699-29 cw ring dye laser. It is pumped with the 514 nm line of a Coherent Innova Sabre argon ion laser. Approximately 7.9 W of pump power produces 100–400 mW of dye laser power with a wavelength tuning range of 720–775 nm using the dye LDS 722. With the frequency of the Ti:Sapphire laser fixed on the pump transition, the probe laser frequency was scanned while monitoring the anode current from a freestanding Hamamatsu R928

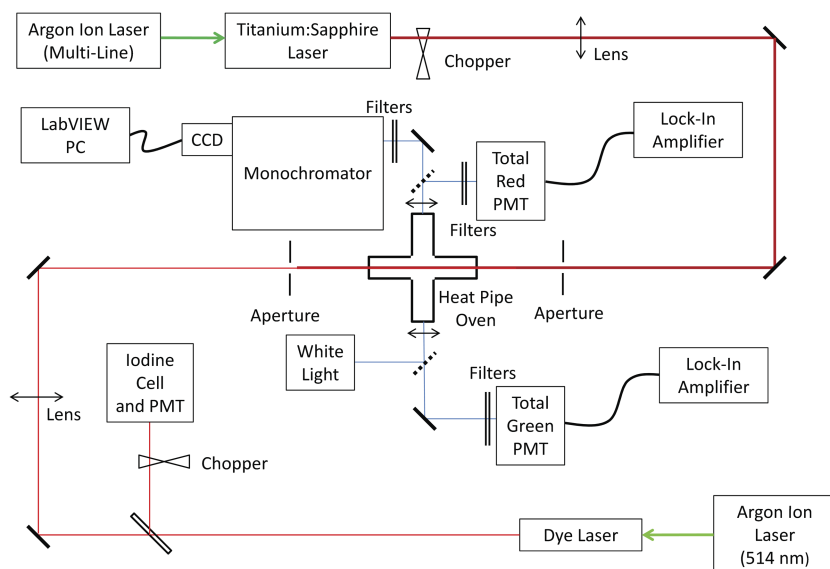


FIG. 1. Schematic diagram of the apparatus used in this work. Solid diagonal lines represent fixed mirrors while dashed diagonal lines represent removable mirrors. Double headed arrows indicate lenses.

photomultiplier tube (“Total Green PMT” in Fig. 1) that was filtered to pass green light using a stack of short pass filters with cutoff wavelengths of 575, 650, 675, 700, and 800 nm (Reynard Corporation R00920-00, R00940-00, R00942-00, R00944-00, and Melles Griot 03SW618, respectively). The probe laser excited transitions from the pumped level of the intermediate state to levels of high-lying electronic states [$^{1,3}\Lambda_{\Omega}(v_{\Lambda}, J_{\Lambda} = J \pm 1) \leftarrow 1(b)^3\Pi(v_b, J) \sim 2(A)^1\Sigma^+(v_A, J)$]. The beams from the two lasers counterpropagated through the heat pipe oven and were focused to spot sizes of ~ 1 mm diameter at the center of the oven.

The pump laser induced transitions from a thermally populated ro-vibrational level of the ground state [$1(X)^1\Sigma^+$] to a selected level of the mixed $1(b)^3\Pi \sim 2(A)^1\Sigma^+$ states. Strong spin-orbit interactions cause every ro-vibrational level of the $1(b)^3\Pi \sim 2(A)^1\Sigma^+$ manifold to have both singlet and triplet characters. Hence the laser in the probe step was able to induce transitions either to upper singlet states or to upper triplet states. Double resonance transitions were observed by detecting fluorescence corresponding to transitions from the upper state down to either the $1(a)^3\Sigma^+$ state or the $1(X)^1\Sigma^+$ state as a function of probe laser frequency (with pump laser frequency fixed) or as a function of pump laser frequency (with probe frequency fixed). In order to distinguish double resonance molecular fluorescence from various background light sources, the fixed-frequency laser beam was chopped, and lock-in detection was used.

The frequencies of transitions excited by the Ti:Sapphire laser were calibrated by comparison of the wavemeter readout to lines in the uranium atlas⁵⁷ or to previously calibrated NaCs $2(A)^1\Sigma^+(v_A, J) \leftarrow 1(X)^1\Sigma^+(v_X, J \pm 1)$ transitions. In the former case, a small part of the beam was split off and sent into a uranium hollow cathode lamp, where the optogalvanic signal was monitored. The Ti:Sapphire wavemeter readout of a particular uranium line was compared to the known frequency in the uranium atlas to determine the offset error of the wavemeter. Once the error was known, unique total red fluorescence signals, recorded as the laser scanned over a set of NaCs $2(A)^1\Sigma^+(v_A, J) \leftarrow 1(X)^1\Sigma^+(v_X, J \pm 1)$ transitions (laser excitation scans), were used for subsequent calibrations. Dye laser transitions were similarly calibrated using fluorescence from an iodine cell, which was compared with line positions tabulated in the iodine atlas.⁵⁸ We believe that $2(A)^1\Sigma^+$ level energies are determined to within ~ 0.01 cm^{-1} , while level energies of electronic states accessed via double resonance are determined to an absolute accuracy of ~ 0.02 cm^{-1} .

With both pump and probe lasers fixed on a double resonance transition, the resolved fluorescence can be used to identify the upper electronic state excited by the transition. Experimentally, the fluorescence is focused onto the entrance slit of a monochromator (Spex 270M, labeled “Monochromator” in Fig. 1) using a lens and mirrors mounted in a periscope arrangement. The monochromator diffraction grating has 600 grooves/mm and is blazed for 1 μm . Typically, the monochromator was used in second-order.

The exit slit of the monochromator was replaced by a charge-coupled device (CCD) array detector. The CCD array is advantageous since it records fluorescence from all wavelengths at the same time. Therefore, a laser frequency drift or

change in laser power will only affect the observed spectrum by an overall intensity-scaling factor. To determine the detection system efficiency as a function of wavelength, a quartz-iodine tungsten filament lamp (GTE Sylvania model 6.6A/T4Q/1CL-200W) was used as a light source with a calibrated standard relative intensity.⁵⁹

The number of ro-vibrational levels that can be probed from a given intermediate state level is limited by the selection rule $\Delta J = \pm 1$, since $\Delta J = 0$ transitions are forbidden for $0^+ \leftrightarrow 0^+$ electronic transitions. A very useful technique to expand the ro-vibrational coverage of the data set is to use observations of collisional satellite lines to assign many rotational levels of a single vibrational state within a single scan of the probe laser. If the atomic argon and/or cesium vapor pressure is sufficiently high, one can observe regularly spaced satellite lines on either side of the directly pumped P and R lines in a pump or probe scan, which (in the case of NaCs)⁶⁰ decrease in intensity with increasing displacement in frequency from the directly excited line. Figure 2 shows a probe laser excitation spectrum with collisional satellite lines. The satellite lines on either side of the direct lines are due to probe transitions out of collisionally populated levels near the intermediate state ro-vibrational level involved in the direct transition. A collision of the molecule in the pumped intermediate level with an atomic collision partner, i.e., $\text{NaCs}[2(A)^1\Sigma^+(v_A, J)] + (\text{Ar or Cs}) \rightarrow \text{NaCs}[2(A)^1\Sigma^+(v_A, J + \Delta J)] + (\text{Ar or Cs})$, causes transfer of population to a nearby rotational level $J + \Delta J$. Reference 52 discusses the identification and determination of the absolute energies of levels associated with the OODR collisional satellite lines in more detail.

This process of identifying collisional lines greatly improves the efficiency with which one can determine level energies, since it is possible to observe transitions to many rotational levels within a single scan. Splittings between rotational levels within an excited NaCs electronic state are typically

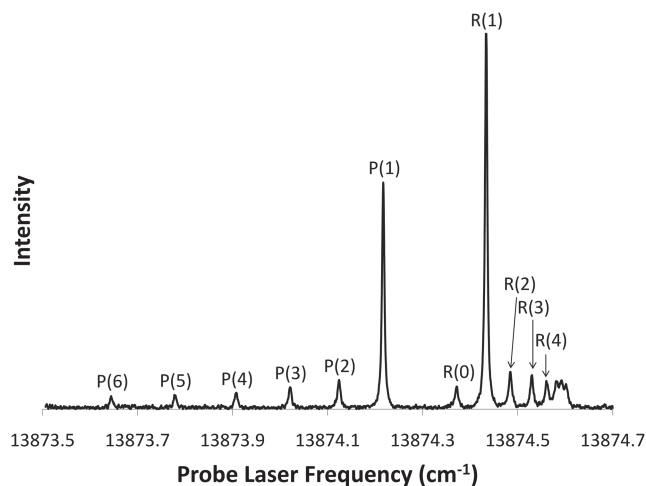


FIG. 2. Example of collisional lines in an OODR excitation spectrum obtained with the pump laser fixed on the NaCs $2(A)^1\Sigma^+(14, 1) \leftarrow 1(X)^1\Sigma^+(0, 2)$ transition. Neighboring lines show probe laser transitions from nearby collisionally populated rotational levels. The probe laser line labeled P(1) shows a transition to a $J = 0$ level of the upper [$12(0^+)$] state. There are no collisional lines associated with the P-series at energies above this line, indicating that the direct P-line [P(1)] does indeed correspond to the lowest possible J value of the upper state [$J = 0$]. This confirms the 0^+ symmetry of the $12(0^+)$ state.

about $2\text{--}6\text{ cm}^{-1}$. However, the spacings between the collisional lines in a single pump or probe laser scan are equal to the *difference* in the rotational splittings of the two electronic states involved in the transition, which is typically on the order of 1 cm^{-1} or less. The collisional lines also allow one to make large jumps in J for pump or probe transitions. These collisional lines are observed by fixing one of the laser frequencies on a collisional peak and scanning the other laser until it becomes resonant with the direct transition for that value of J . Now this new rotational transition can serve as the direct line and new collisional lines are strong enough to assign and expand the rotational level data set.

III. THE NaCs $12(0^+)$ POTENTIAL

In addition to ro-vibrational levels from the NaCs $11(0^+)$ electronic state [$5^3\Pi_{0^+}$ in Hund's case (*a*) notation] that was mapped out previously in our lab,⁵² we have also observed ro-vibrational levels from a second electronic state within the same general energy range, which we have now identified as the NaCs $12(0^+)$ electronic state.

In previous work on NaK,^{61–65} upper triplet states were identified relatively easily by their hyperfine structure that was observed in the probe step of a perturbation-facilitated OODR (PFOODR)⁶⁶ excitation scheme. In our studies of NaCs thus far, we have not observed any hyperfine structure. Arguments based on angular momenta vector coupling models provide an explanation for why hyperfine splittings should be quite small for most electronic states of NaCs.⁵² Therefore, in NaCs, we distinguish ro-vibrational levels of different electronic states by qualitative differences in the associated bound-free fluorescence spectra. The right hand side of Fig. 3 (region above 490 nm) shows NaCs $12(0^+) \rightarrow 1(a^3\Sigma^+)$ bound-free spectra corresponding to different ro-vibrational levels of the upper $12(0^+)$ electronic state. Although the bound-free portions of these spectra are similar to bound-free $5^3\Pi_{0^+} \rightarrow 1(a^3\Sigma^+)$ [$11(0^+) \rightarrow 1(a^3\Sigma^+)$] fluorescence (see Fig. 3 of Ref. 52), the intensity distributions are clearly distinguishable. In addition, the very regular $5^3\Pi_{0^+} \rightarrow 1(a^3\Sigma^+)$ bound-free intensity patterns made it easy to assign upper state vibrational quantum numbers from a simple counting of nodes in the spectra. However, as will be shown below, the intensity distributions of the $12(0^+) \rightarrow 1(a^3\Sigma^+)$ bound-free spectra are much more complex and do not allow vibrational assignments to be made in this fashion. Nevertheless, we found that the low-lying vibrational levels of the $11(0^+)$ and $12(0^+)$ states lie in approximately the same energy region, requiring that the two potential curves must have minima within a few hundred cm^{-1} of each other.

As described in Sec. II, we used optical-optical double resonance (OODR) spectroscopy to measure energies for many ro-vibrational levels of the NaCs $12(0^+)$ state. Use of collisional lines provides good coverage of rotational levels and allows pump transitions with different J values to be identified quickly. Using the pump transitions $2(A)^1\Sigma^+(14,1) \leftarrow 1(X)^1\Sigma^+(0,2)$ and $2(A)^1\Sigma^+(14,1) \leftarrow 1(X)^1\Sigma^+(0,0)$, we were able to excite the probe transition $12(0^+)(v=12, J=0) \leftarrow 2(A)^1\Sigma^+(14,1)$ (see Fig. 2), thereby verifying the $\Omega=0$ and + symmetries of the upper state.

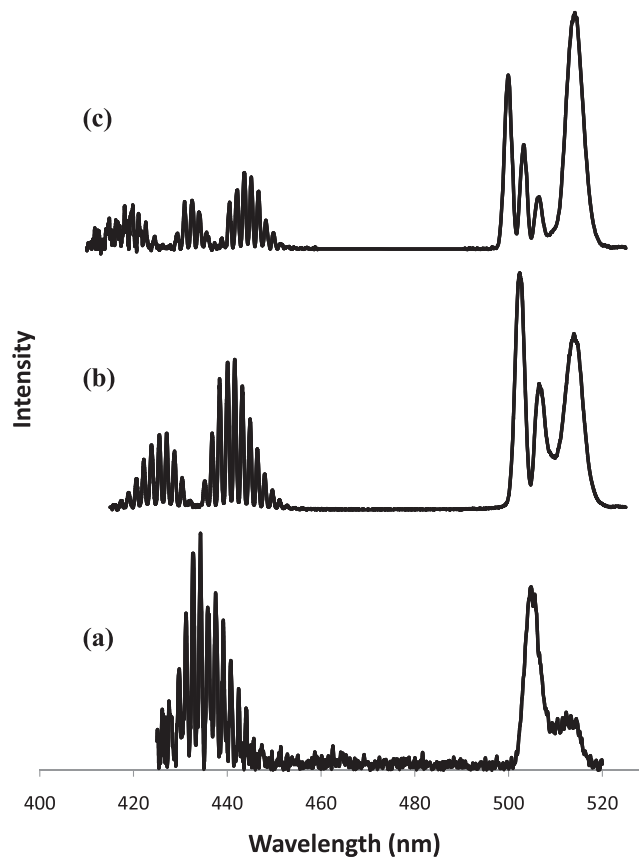


FIG. 3. Experimental NaCs $12(0^+) \rightarrow 1(X)^1\Sigma^+$ bound-bound and $12(0^+) \rightarrow 1(a^3\Sigma^+)$ bound-free resolved fluorescence spectra associated with the three lowest vibrational levels of the NaCs $12(0^+)$ state. Upper state vibrational and rotational quantum numbers are (a) (0, 43), (b) (1, 43), and (c) (2, 43). Vibrational quantum number assignments are explained in Sec. IV. The $12(0^+) \rightarrow 1(X)^1\Sigma^+$ bound-bound fluorescence appears as a series of discrete vibrational peaks in the 410–460 nm region, while the $12(0^+) \rightarrow 1(a^3\Sigma^+)$ bound-free continuum fluorescence is observed in the 500–520 nm region. Each spectrum has been corrected for the wavelength dependence of the detection system efficiency, resulting in an increase in the apparent noise level at the short wavelength end of each spectrum.

From progressions of ro-vibrational levels, which display bound-free spectra similar to those shown in Fig. 3, preliminary values for molecular constants, $T_e \approx 24\,670\text{ cm}^{-1}$, $\omega_e \approx 54\text{ cm}^{-1}$, and $B_e \approx 0.036\text{ cm}^{-1}$, which corresponds to an equilibrium separation of $R_e \approx 4.9\text{ \AA}$, were obtained for the $12(0^+)$ state. These values are quite similar to those of the $11(0^+)$ state, for which Ashman *et al.*⁵² found $T_e = 24\,511.8\text{ cm}^{-1}$, $\omega_e = 64.24\text{ cm}^{-1}$, $B_e = 0.037\,06\text{ cm}^{-1}$, and $R_e = 4.8\text{ \AA}$. Comparison with the theoretical potentials of Korek *et al.*⁵⁵ shows that these two observed states must be $11(0^+)$ and $12(0^+)$. However, we note that the theoretical calculations of Korek *et al.*⁵⁵ identified the $7^1\Sigma^+$ state as $11(0^+)$ and $5^3\Pi_{0^+}$ as $12(0^+)$, whereas experimentally we find that the predominantly singlet state [$7^1\Sigma^+$] lies slightly higher in energy than the predominantly triplet state [$5^3\Pi_{0^+}$]. Note that the $5^3\Pi_{0^+}$ state was identified in Ref. 52 as $12(0^+)$ based on the assignments of Korek *et al.*⁵⁵ However, based on the current analysis, the state labeled $5^3\Pi_{0^+}$ should be identified as $11(0^+)$ and the state labeled $7^1\Sigma^+$ as $12(0^+)$.

For the $11(0^+)$ state, the vibrational quantum number assignment was straightforward since the bound-free

spectra, presented in Fig. 3 of Ref. 52, are not complicated. For transitions between states with a difference potential that is monotonic in R , the vibrational quantum number can be assigned from the bound-free spectra, which display $v + 1$ maxima. Unfortunately, the bound-free spectra associated with the $12(0^+)$ state are not as simple and an absolute vibrational numbering could not be determined using the bound-free emission spectra alone. The reasons for this are discussed in Sec. IV. However, because the $12(0^+)$ state has both singlet and triplet characters, the resolved fluorescence spectrum that corresponds to each ro-vibrational level of this state is composed of two parts: $12(0^+) \rightarrow 1(a)^3 \Sigma^+$ bound-free fluorescence and $12(0^+) \rightarrow 1(X)^1 \Sigma^+$ bound-bound fluorescence (see Fig. 3). The envelope of the bound-bound $12(0^+) \rightarrow 1(X)^1 \Sigma^+$ fluorescence does display $v + 1$ maxima and can, therefore, be used to obtain a definite assignment of the $12(0^+)$ vibrational quantum numbers of the lowest vibrational levels. Once the vibrational numbering of the low-lying levels was established, it was easy to assign all other measured ro-vibrational levels.

As a first step in constructing an experimental potential energy curve for the NaCs $12(0^+)$ state, we used Le Roy's DParFit computer program⁶⁷ to fit all measured level energies to a set of Dunham coefficients,

$$E(v, J) = \sum_{i,k} Y_{i,k} \left(v + \frac{1}{2} \right)^i [J(J+1) - \Omega^2]^k \quad (1)$$

with $\Omega = 0$ for the $12(0^+)$ state. Preliminary fits of rotational constants had indicated that the centrifugal distortion constant, D_v , was constant with respect to v to within uncertainties. Therefore, we fixed $Y_{0,2}$ to the value $-6.14 \times 10^{-8} \text{ cm}^{-1}$, which was the average value of $-D_v$ obtained from quadratic fits of $E(v, J) = T_e + G_v + B_v J(J+1) - D_v [J(J+1)]^2$ vs. $J(J+1)$ for vibrational levels where we had observed long rotational progressions ($v = 1, 2, 4, 5$, and 6). 214 level energies spanning a range of vibrational levels $v = 0-14$ were used in the Dunham fit and the best set of Dunham coefficients is listed in Table I. These coefficients reproduce the level energies with a root mean square (RMS) deviation of 0.38 cm^{-1} .

We used the Dunham coefficients to construct a preliminary NaCs $12(0^+)$ electronic potential energy curve using the Rydberg-Klein-Rees⁶⁸⁻⁷⁰ method and the computer program RKR1 2.0, developed by Robert Le Roy.⁷¹ The RMS deviation between measured level energies and energies calculated from this RKR potential using LEVEL 8.0⁷² was 0.65 cm^{-1} for

TABLE I. NaCs $12(0^+)$ state Dunham coefficients. All coefficients are in units of cm^{-1} . The number of digits reported is in some cases larger than warranted by statistical significance. However, they are necessary to reproduce experimental energies to within the stated accuracy.

i	k		
	0	1	2
0	$24\,671.02 \pm 0.57$	$(3.683 \pm 0.021) \times 10^{-2}$	-6.14×10^{-8} (fixed)
1	44.24 ± 0.42	$(1.95 \pm 0.84) \times 10^{-4}$...
2	2.694 ± 0.11	$(-2.41 \pm 0.68) \times 10^{-5}$...
3	$-0.273\,42 \pm 0.011$
4	$(8.57 \pm 0.37) \times 10^{-3}$

$v = 0-14$ vibrational levels. This RKR potential, which is listed in the [supplementary material](#), was used as the starting point to apply the Inverted Perturbation Approach (IPA) to obtain a more accurate potential.

The NaCs $12(0^+)$ RKR potential fails to reproduce the level energies to within the accuracy with which they were measured. The IPA⁷³ process starts with an initial potential, $V_0(R)$, and adds a correction term $\delta V(R)$ to it; $V(R) = V_0(R) + \delta V(R)$. The correction term is expressed as an expansion over a set of basis functions $f_i(R)$,

$$\delta V(R) = \sum_i c_i f_i(R), \quad (2)$$

and the expansion coefficients c_i are obtained using first-order perturbation theory to calculate energy corrections

$$\begin{aligned} \delta E_{v,J} &= \int \xi_{v,J}^0(R) \delta V(R) \xi_{v,J}^0(R) dR \\ &= \sum_i c_i \int \xi_{v,J}^0(R) f_i(R) \xi_{v,J}^0(R) dR \equiv \sum_i c_i K_{i;v,J}, \end{aligned} \quad (3)$$

where the $\xi_{v,J}^0(R)$ are the radial wavefunctions corresponding to the zeroth-order potentials $V_0(R)$. Using the last equality of Eq. (3), the energy corrections can be written in matrix form as

$$\delta \mathbf{E} = \mathbf{c} \cdot \mathbf{K}. \quad (4)$$

The energy corrections are the differences between the measured energies $E_{v,J}^{\text{meas}}$ and the zeroth-order calculated energies $E_{v,J}^0$ [eigenvalues of $V_0(R)$], and the elements of the \mathbf{K} matrix are calculated using the zeroth-order radial wavefunctions. Thus the only unknown quantities are the expansion coefficients for the correction potential c_i (elements of the \mathbf{c} matrix). These coefficients are varied until the elements of $\delta \mathbf{E}$ are minimized in a least squares sense.

In practice, we used a modified version⁶³ of the IPA program written by Pashov *et al.*⁷⁴ The IPA program requires as input the experimental energies of measured ro-vibrational levels along with experimental uncertainties, the initial potential curve used in that iteration, and the calculated energies and wavefunctions for the initial potential. We used the program xLEVEL, which is a version of Le Roy's LEVEL program that was slightly modified by Hickman (see Ref. 62), to calculate the energies and wavefunctions. The RKR potential, described above, served as the initial potential, $V_0(R)$, in the first iteration. The correction potential $\delta V(R)$ is defined on an equally spaced grid of points in R . However, the number of grid points to use in a given iteration and whether the potential is allowed to vary at a particular grid point in that iteration are chosen by the user. After each iteration of the IPA potential, the new potential $V(R) = V_0(R) + \delta V(R)$ was calculated at the grid points and then splined. Energies and wavefunctions for the new potential were calculated using xLEVEL, which along with the new potential, served as input for the next iteration of IPA. This process was iterated until level energies calculated using the new $V(R)$ were in sufficient agreement with measured level energies.

Use of a progressively finer grid of points will continue to reduce discrepancies between calculated and measured energies, but at the expense of unphysical wiggles in the potential.

The “best” fit IPA potential was determined by us as a trade-off between accurate reproduction of level energies while still maintaining a reasonably smooth potential. Using these criteria, we determined our best fit IPA potential for the NaCs $12(0^+)$ state, which is shown in Fig. 4 and listed in Table II. The initial RKR potential was calculated with turning points up to $v = 14$. However, the levels corresponding to $v = 12, 13$, and 14 appear to be strongly perturbed so they were not used for the fitting of the IPA potential, which reproduces measured level energies for $v = 0-10$ with an RMS deviation of 0.034 cm^{-1} . A plot of the differences between the observed energies and those calculated using the IPA potential is given in the [supplementary material](#).

When comparing the IPA potential to theoretical or RKR potentials, it is clear that the IPA potential is not a simple smooth curve. Some “wiggles” in the inner and outer IPA potential walls appear to be necessary in order to accurately reproduce the level energies. This is a result of our implicit assumption that all of the measured energy levels of the $12(0^+)$ state can be described by a single potential energy curve. In reality, there are other NaCs electronic state potential curves in this energy region that interact with the $12(0^+)$ state, thus influencing the patterns of ro-vibrational level energies. Specifically, the $11(0^+)$ electronic state, which was previously mapped by Ashman *et al.*,⁵² shows similar fluctuations in its outer wall. In Sec. IV, we discuss how these two states probably interact and how this interaction influences not only the level energies but also the vibrational wavefunctions, and hence, the resolved fluorescence spectra associated with these states.

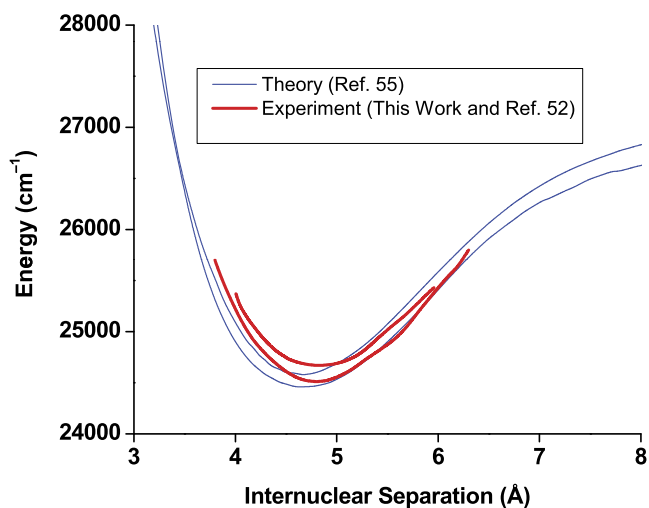


FIG. 4. Experimental IPA potential for the NaCs $12(0^+)$ state determined in this work along with the experimental potential for the NaCs $11(0^+)$ state from Ref. 52 (upper and lower thick red lines, respectively) and the NaCs $12(0^+)$ and $11(0^+)$ theoretical potentials of Korek *et al.*⁵⁵ (upper and lower thin blue curves, respectively). The Korek *et al.* ground state well depth is larger by 298.214 cm^{-1} than the experimental ground state well depth of Ref. 44. Since the T_e values reported in Ref. 55 are based on energies relative to the bottom of this theoretical ground state potential, while our experimental $11(0^+)$ and $12(0^+)$ potentials are referenced to the bottom of the experimental ground state potential of Ref. 44, we have shifted the theoretical curves down by 298.214 cm^{-1} so that the ground state asymptotes of the theoretical and experimental potentials coincide. We believe this makes the comparison of the theoretical and experimental potentials more meaningful.

TABLE II. NaCs $12(0^+)$ IPA potential energy curve determined in this work.

R (Å)	Energy (cm^{-1})	R (Å)	Energy (cm^{-1})
4.0066	25 372.1902	4.9204	24 675.7057
4.0120	25 353.8388	4.9832	24 685.5888
4.0249	25 313.6700	5.0252	24 694.8413
4.0447	25 262.8959	5.0586	24 704.7210
4.0702	25 212.3998	5.0870	24 715.0111
4.1006	25 162.1021	5.1119	24 725.0570
4.1349	25 112.1539	5.1344	24 734.6046
4.1727	25 061.5645	5.1549	24 743.7734
4.2137	25 009.3151	5.1740	24 752.9083
4.2583	24 955.1027	5.1919	24 762.1829
4.2773	24 933.1528	5.2089	24 773.3190
4.2871	24 922.2078	5.2250	24 783.9433
4.2971	24 911.3020	5.2405	24 794.7367
4.3073	24 900.4408	5.2554	24 805.6899
4.3178	24 889.6251	5.2698	24 816.7863
4.3285	24 878.8374	5.2838	24 828.0196
4.3395	24 868.0960	5.2975	24 839.3859
4.3508	24 857.3999	5.3109	24 850.8537
4.3625	24 846.7576	5.3241	24 862.3620
4.3745	24 836.1676	5.3370	24 873.8740
4.3870	24 825.6479	5.3498	24 885.3510
4.3999	24 815.1958	5.3624	24 896.7747
4.4134	24 804.8180	5.3750	24 908.1083
4.4274	24 794.5197	5.3874	24 919.3482
4.4422	24 784.2999	5.3998	24 930.4736
4.4577	24 774.1712	5.4121	24 941.4632
4.4741	24 764.1546	5.4366	24 962.9916
4.4916	24 754.2386	5.4977	25 014.7877
4.5104	24 739.9024	5.5593	25 065.4399
4.5308	24 730.5804	5.6216	25 115.7452
4.5531	24 721.3148	5.6844	25 169.3976
4.5780	24 712.0850	5.7468	25 228.9479
4.6064	24 702.7850	5.8073	25 288.2247
4.6399	24 693.3421	5.8644	25 344.1242
4.6820	24 683.7029	5.9159	25 391.9912
4.7449	24 673.2199	5.9603	25 430.4357
4.8327	24 668.2803		

IV. INTERACTIONS BETWEEN THE NaCs $11(0^+)$ AND $12(0^+)$ STATES

Although the $12(0^+)$ electronic state has predominantly singlet character, resolved fluorescence spectra from this electronic state show strong bound-free emission to the $1(a)^3\Sigma^+$ electronic state. We believe this is due to the interaction of the $12(0^+)$ state with the $11(0^+)$ state, which has predominantly triplet character. However, by itself, the spin-orbit interaction between these two states is not sufficient to explain the observed intensity distribution in the $12(0^+) \rightarrow 1(a)^3\Sigma^+$ bound-free emission spectra. In the following, we describe a model for certain types of interactions between electronic states that we believe to be responsible for the unique intensity distributions of the $12(0^+) \rightarrow 1(a)^3\Sigma^+$ bound-free emission.

A. Model for spin-orbit and non-adiabatic interactions between the NaCs $11(0^+)$ and $12(0^+)$ states

The $12(0^+) \rightarrow 1(a)^3\Sigma^+$ electronic transition displays very well resolved and distinctive bound-free fluorescence

spectra (see Fig. 3, right hand side). However, the $12(0^+) \rightarrow 1(X)^1\Sigma^+$ electronic transition is also strong, and we observe clean bound-bound spectra associated with this fluorescence channel (Fig. 3, left hand side). The fact that the $12(0^+)$ state makes radiative transitions down to both the repulsive triplet state, $1(a)^3\Sigma^+$, and to the singlet ground state, $1(X)^1\Sigma^+$, indicates that the $12(0^+)$ state has both triplet and singlet characters. This is most likely due to spin-orbit perturbations by the nearby $11(0^+)$ electronic state, which is labeled $5^3\Pi_{0^+}$ in Hund's case (*a*) notation. In theoretical calculations, which do not include the spin-orbit effect,⁵⁴ the $12(0^+)$ state is labeled $7^1\Sigma^+$ in the case (*a*) designation. Spin-orbit interactions between $^3\Pi$ and $^1\Sigma$ states are very common,⁷ so it is likely that each of the ro-vibrational levels of both states has significant singlet and triplet characters due to the mixing of the electronic wavefunctions. However, if it is assumed that the singlet component of the mixed state wavefunction is entirely responsible for the bound-bound fluorescence, and the triplet component is entirely responsible for the bound-free fluorescence, then it is clear from the $12(0^+) \rightarrow 1(a)^3\Sigma^+$ bound-free intensity distribution that the spin-orbit effect cannot be the only $11(0^+)$ – $12(0^+)$ interaction responsible for the mixing of the levels of these two electronic states.

In the case of NaCs, the intensity distributions in the $11(0^+) \rightarrow 1(a)^3\Sigma^+$ and $12(0^+) \rightarrow 1(a)^3\Sigma^+$ resolved bound-free fluorescence spectra are qualitatively very different for nearby ro-vibrational levels of the two upper states. To explain the different intensity distributions of the bound-free emission, we have developed a model based on two separate interaction mechanisms between these states, which we describe here.

First, we consider the electronic part of the wavefunctions describing levels of the $11(0^+)$ and $12(0^+)$ states. One key assumption of this model is that only these two electronic states interact strongly with each other via spin-orbit interactions. Discussion of the validity of assumptions used in the model is deferred to Sec. IV C. However using this two-state assumption, we can write the relativistic [Hund's case (*c*), spin-orbit included] electronic wavefunctions $[\Phi_{11(0^+)}(\vec{r}, R), \Phi_{12(0^+)}(\vec{r}, R)]$ in terms of the non-relativistic [Hund's case (*a*), spin-orbit neglected] electronic wavefunctions $[\Phi_{5^3\Pi_{0^+}}(\vec{r}, R), \Phi_{7^1\Sigma^+}(\vec{r}, R)]$ as

$$\Phi_{12(0^+)}(\vec{r}, R) = \cos \theta(R)\Phi_{7^1\Sigma^+}(\vec{r}, R) + \sin \theta(R)\Phi_{5^3\Pi_{0^+}}(\vec{r}, R) \quad (5)$$

and

$$\Phi_{11(0^+)}(\vec{r}, R) = -\sin \theta(R)\Phi_{7^1\Sigma^+}(\vec{r}, R) + \cos \theta(R)\Phi_{5^3\Pi_{0^+}}(\vec{r}, R). \quad (6)$$

The expansion coefficients are written using sines and cosines so that normalization is automatically satisfied. However, we allow for the possibility that the mixing angle depends (perhaps strongly) on internuclear separation, R . This analysis of the mixing of the electronic wavefunctions emphasizes the fact that, in NaCs, the large spin-orbit effect causes global perturbations that affect *all levels of both electronic states*.

In addition to the mixing of the electronic state wavefunctions due to the spin-orbit interaction, we assume that a

particular ro-vibrational level (v_{12}, J) of the $12(0^+)$ state can also interact (we believe indirectly) with one particular ro-vibrational level (v_{11}, J) of the $11(0^+)$ state via some separate, weaker interaction. We believe this interaction is a second-order, non-adiabatic coupling involving the complete set of vibrational levels of a third electronic state. The proposed mechanism explains why interactions between levels v_{12} and v_{11} are strongly favored when $v_{11} = v_{12} + 2$, which is consistent with the experimental results presented below.

Non-adiabatic interactions are caused by nuclear kinetic energy terms that are neglected when the Born-Oppenheimer approximation is invoked. We start by evaluating the off-diagonal Hamiltonian matrix element of the nuclear kinetic energy operator between level v_{11} of the $11(0^+)$ adiabatic state and level v_{12} of the $12(0^+)$ adiabatic state

$$H_{v_{11}, v_{12}} = \langle \Phi_{11}^{ad} \chi_{v_{11}}^{ad} | \mathbf{T}^N | \Phi_{12}^{ad} \chi_{v_{12}}^{ad} \rangle \quad (7)$$

with

$$\begin{aligned} \mathbf{T}^N &= -\frac{\hbar^2}{2\mu R^2} \left\{ \frac{\partial}{\partial R} \left[R^2 \frac{\partial}{\partial R} \right] - \mathbf{R}^2 \right\} \\ &= -\frac{\hbar^2}{2\mu} \left[\frac{\partial^2}{\partial R^2} + \frac{2}{R} \frac{\partial}{\partial R} \right] + \frac{\hbar^2}{2\mu R^2} \mathbf{R}^2. \end{aligned} \quad (8)$$

In the above expression, R is the internuclear separation and $\mathbf{R} = \mathbf{J} - \mathbf{L} - \mathbf{S}$ is the nuclear rotation angular momentum. The nuclear rotation term is small compared to the radial terms and can be neglected (see Ref. 7, page 168).

Next, we calculate

$$\begin{aligned} \mathbf{T}^N (\Phi_{12}^{ad} \chi_{v_{12}}^{ad}) &= -\frac{\hbar^2}{2\mu} \left[\frac{\partial^2 (\Phi_{12}^{ad} \chi_{v_{12}}^{ad})}{\partial R^2} + \frac{2}{R} \frac{\partial (\Phi_{12}^{ad} \chi_{v_{12}}^{ad})}{\partial R} \right] \\ &= -\frac{\hbar^2}{2\mu} \left[\chi_{v_{12}}^{ad} \frac{\partial^2 \Phi_{12}^{ad}}{\partial R^2} + \Phi_{12}^{ad} \frac{\partial^2 \chi_{v_{12}}^{ad}}{\partial R^2} \right. \\ &\quad + 2 \frac{\partial \Phi_{12}^{ad}}{\partial R} \frac{\partial \chi_{v_{12}}^{ad}}{\partial R} + \frac{2}{R} \chi_{v_{12}}^{ad} \frac{\partial \Phi_{12}^{ad}}{\partial R} \\ &\quad \left. + \frac{2}{R} \Phi_{12}^{ad} \frac{\partial \chi_{v_{12}}^{ad}}{\partial R} \right] \end{aligned} \quad (9)$$

and the matrix element

$$\begin{aligned} H_{v_{11}, v_{12}} &= \langle \Phi_{11}^{ad} \chi_{v_{11}}^{ad} | \mathbf{T}^N | \Phi_{12}^{ad} \chi_{v_{12}}^{ad} \rangle \\ &= -\frac{\hbar^2}{2\mu} \int \int d^3 R d^3 r (\chi_{v_{11}}^{ad})^* (\Phi_{11}^{ad})^* \\ &\quad \times \left[\chi_{v_{12}}^{ad} \frac{\partial^2 \Phi_{12}^{ad}}{\partial R^2} + \Phi_{12}^{ad} \frac{\partial^2 \chi_{v_{12}}^{ad}}{\partial R^2} + 2 \frac{\partial \Phi_{12}^{ad}}{\partial R} \frac{\partial \chi_{v_{12}}^{ad}}{\partial R} \right. \\ &\quad \left. + \frac{2}{R} \chi_{v_{12}}^{ad} \frac{\partial \Phi_{12}^{ad}}{\partial R} + \frac{2}{R} \Phi_{12}^{ad} \frac{\partial \chi_{v_{12}}^{ad}}{\partial R} \right]. \end{aligned} \quad (10)$$

Only the electronic wavefunctions depend on the electron coordinates \vec{r} , and these electronic wavefunctions are orthogonal. Therefore we can eliminate the terms involving $\langle \Phi_{11}^{ad} | \Phi_{12}^{ad} \rangle$; i.e., the 2nd and 5th terms in this expression,

$$H_{v_{11},v_{12}} = -\frac{\hbar^2}{2\mu} \int \int d^3R d^3r (\chi_{v_{11}}^{ad})^* (\Phi_{11}^{ad})^* \left[\chi_{v_{12}}^{ad} \frac{\partial^2 \Phi_{12}^{ad}}{\partial R^2} + 2 \frac{\partial \Phi_{12}^{ad}}{\partial R} \frac{\partial \chi_{v_{12}}^{ad}}{\partial R} + \frac{2}{R} \chi_{v_{12}}^{ad} \frac{\partial \Phi_{12}^{ad}}{\partial R} \right]. \quad (11)$$

Introducing $\chi_v^{ad} = \frac{\xi_v^{ad}}{R}$ and the fact that the rotational (nuclear angular) wavefunctions are described by spherical harmonics, which are orthonormal, we can write

$$\begin{aligned} H_{v_{11},v_{12}} &= -\frac{\hbar^2}{2\mu} \int \int R^2 dR d^3r \left(\frac{\xi_{v_{11}}^{ad}}{R} \right)^* (\Phi_{11}^{ad})^* \left[\frac{\xi_{v_{12}}^{ad}}{R} \frac{\partial^2 \Phi_{12}^{ad}}{\partial R^2} + 2 \frac{\partial \Phi_{12}^{ad}}{\partial R} \frac{\partial (\xi_{v_{12}}^{ad}/R)}{\partial R} + \frac{2}{R} \frac{\xi_{v_{12}}^{ad}}{R} \frac{\partial \Phi_{12}^{ad}}{\partial R} \right] \\ &= -\frac{\hbar^2}{2\mu} \int \int dR d^3r (\xi_{v_{11}}^{ad})^* (\Phi_{11}^{ad})^* \left[\xi_{v_{12}}^{ad} \frac{\partial^2 \Phi_{12}^{ad}}{\partial R^2} + 2 \frac{\partial \Phi_{12}^{ad}}{\partial R} \frac{\partial \xi_{v_{12}}^{ad}}{\partial R} - \frac{2}{R} \xi_{v_{12}}^{ad} \frac{\partial \Phi_{12}^{ad}}{\partial R} + \frac{2}{R} \xi_{v_{12}}^{ad} \frac{\partial \Phi_{12}^{ad}}{\partial R} \right] \\ &= -\frac{\hbar^2}{2\mu} \int \int dR d^3r (\xi_{v_{11}}^{ad})^* (\Phi_{11}^{ad})^* \left[\xi_{v_{12}}^{ad} \frac{\partial^2 \Phi_{12}^{ad}}{\partial R^2} + 2 \frac{\partial \Phi_{12}^{ad}}{\partial R} \frac{\partial \xi_{v_{12}}^{ad}}{\partial R} \right] \\ &= -\frac{\hbar^2}{2\mu} \int \int dR d^3r (\Phi_{11}^{ad})^* \left[\xi_{v_{11}}^{ad} \xi_{v_{12}}^{ad} \frac{\partial^2 \Phi_{12}^{ad}}{\partial R^2} + 2 \xi_{v_{11}}^{ad} \frac{\partial \Phi_{12}^{ad}}{\partial R} \frac{\partial \xi_{v_{12}}^{ad}}{\partial R} \right]. \end{aligned} \quad (12)$$

In the last step, we have used the fact that the vibrational wavefunctions are real. In bra-ket notation, this last expression reads

$$\begin{aligned} H_{v_{11},v_{12}} &= -\frac{\hbar^2}{2\mu} \langle \xi_{v_{11}}^{ad} | \langle \Phi_{11}^{ad} | \frac{\partial^2}{\partial R^2} | \Phi_{12}^{ad} \rangle | \xi_{v_{12}}^{ad} \rangle \\ &\quad - \frac{\hbar^2}{\mu} \langle \xi_{v_{11}}^{ad} | \langle \Phi_{11}^{ad} | \frac{\partial}{\partial R} | \Phi_{12}^{ad} \rangle \frac{\partial}{\partial R} | \xi_{v_{12}}^{ad} \rangle. \end{aligned} \quad (13)$$

For reasons that will become apparent below, we believe that the derivative operators do not cause interactions between the 11(0⁺) state and 12(0⁺) state vibrational levels v_{11} and v_{12} directly. Instead, we surmise that the interaction between these vibrational levels must occur indirectly via the complete set of vibrational levels of a third electronic state, which we label as state 3. We propose that these interactions result in mixed vibrational levels

$$\begin{aligned} |\Psi_1\rangle &= a_1 |\Phi_{11}\rangle | \xi_{v_{11}}^J \rangle + \sum_{v_{12}} b_{1,v_{12}} |\Phi_{12}\rangle | \xi_{v_{12}}^J \rangle \\ &\quad + \sum_{v_3} c_{1,v_3} |\Phi_3\rangle | \xi_{v_3}^J \rangle \end{aligned} \quad (14)$$

and

$$\begin{aligned} |\Psi_1\rangle &= a_1 |\Phi_{11}^{ad}\rangle | \xi_{v_{11}}^{ad} \rangle - a_1 \sum_{v_3} \frac{\langle \xi_{v_3}^{ad} | \langle \Phi_3^{ad} | \frac{\partial}{\partial R} | \Phi_{11}^{ad} \rangle | \frac{\partial \xi_{v_{11}}^{ad}}{\partial R} \rangle}{E_{v_{11}} - E_{v_3}^0} |\Phi_3^{ad}\rangle | \xi_{v_3}^{ad} \rangle \\ &\quad + a_1 \frac{\hbar^4}{\mu^2} \sum_{v_{12}} \sum_{v_3} \frac{\langle \frac{\partial \xi_{v_{12}}^{ad}}{\partial R} | \langle \Phi_{12}^{ad} | \frac{\partial}{\partial R} | \Phi_3^{ad} \rangle | \xi_{v_3}^{ad} \rangle \langle \xi_{v_3}^{ad} | \langle \Phi_3^{ad} | \frac{\partial}{\partial R} | \Phi_{11}^{ad} \rangle | \frac{\partial \xi_{v_{11}}^{ad}}{\partial R} \rangle}{(E_{v_{11}} - E_{v_{12}}^0)(E_{v_{11}} - E_{v_3}^0)} |\Phi_{12}^{ad}\rangle | \xi_{v_{12}}^{ad} \rangle + \dots, \end{aligned} \quad (16)$$

where we have considered only the second term in Eq. (13) as responsible for the perturbation interaction and assumed no direct coupling between the 11(0⁺) and 12(0⁺) states due to these derivative terms. Instead, 11(0⁺) and 12(0⁺) each separately interact

$$\begin{aligned} |\Psi_2\rangle &= \sum_{v_{11}} a_{2,v_{11}} |\Phi_{11}\rangle | \xi_{v_{11}}^J \rangle + b_2 |\Phi_{12}\rangle | \xi_{v_{12}}^J \rangle \\ &\quad + \sum_{v_3} c_{2,v_3} |\Phi_3\rangle | \xi_{v_3}^J \rangle. \end{aligned} \quad (15)$$

The 11(0⁺) and 12(0⁺) electronic potential curves are nearly parallel. And in the lowest-order approximation, we can describe their vibrational wavefunctions by harmonic oscillator eigenfunctions. Therefore, assuming that the electronic matrix elements vary slowly with internuclear distance, the first term in Eq. (13) would be largest for $v_{11} = v_{12}$, while the second term in (13) would be largest for $v_{11} = v_{12} \pm 1$. Numerical calculations using wavefunctions calculated from experimental potentials confirm these results. However, our experimental data suggest that the dominant interactions between the 11(0⁺) and 12(0⁺) vibrational levels occur when $v_{11} = v_{12} + 2$. This leads us to believe that the derivative operators in Eq. (13) do not directly couple the 11(0⁺) and 12(0⁺) electronic states, and that *the interaction between them must be mediated by a third electronic state*. As we will show below, the second term in (13) is responsible for the second-order interaction between v_{12} and $v_{11} = v_{12} + 2$.

Second-order perturbation theory [see Subsection 1 of the Appendix, Eq. (A6)] allows us to write the electronic-vibrational wavefunction of level 1, which is of predominantly 11(0⁺) character, as

with state 3. Comparing Eq. (16) to Eq. (14) allows us to identify

$$\frac{b_{1,v_{12}}}{a_1} \approx \frac{\hbar^4}{\mu^2} \sum_{v_3} \frac{\left\langle \frac{\partial \xi_{v_{12}}^{ad}}{\partial R} \left| \langle \Phi_{12}^{ad} \left| \frac{\partial}{\partial R} \right| \Phi_3^{ad} \right\rangle \xi_{v_3}^{ad} \right\rangle \left\langle \xi_{v_3}^{ad} \left| \langle \Phi_3^{ad} \left| \frac{\partial}{\partial R} \right| \Phi_{11}^{ad} \right\rangle \left| \frac{\partial \xi_{v_{11}}^{ad}}{\partial R} \right\rangle}{(E_{v_{11}} - E_{v_{12}}^0) (E_{v_{11}} - E_{v_3}^0)} \quad (17)$$

and

$$\frac{c_{3,v_3}}{a_1} \approx -\frac{\hbar^2}{\mu} \frac{\left\langle \xi_{v_3}^{ad} \left| \langle \Phi_3^{ad} \left| \frac{\partial}{\partial R} \right| \Phi_{11}^{ad} \right\rangle \left| \frac{\partial \xi_{v_{11}}^{ad}}{\partial R} \right\rangle}{E_{v_{11}} - E_{v_3}^0}. \quad (18)$$

Assuming that the energy differences between level v_{11} and the various vibrational levels of the unknown state 3 are all approximately equal, we can use the completeness of the state 3 vibrational wavefunctions $\sum_{v_3} \left\langle \xi_{v_3}^{ad} \left| \xi_{v_3}^{ad} \right\rangle = 1$ to write Eq. (17) as

$$\frac{b_{1,v_{12}}}{a_1} \approx \frac{\hbar^4}{\mu^2} \frac{\left\langle \frac{\partial \xi_{v_{12}}^{ad}}{\partial R} \left| \langle \Phi_{12}^{ad} \left| \frac{\partial}{\partial R} \right| \Phi_3^{ad} \right\rangle \left\langle \Phi_3^{ad} \left| \frac{\partial}{\partial R} \right| \Phi_{11}^{ad} \right\rangle \left| \frac{\partial \xi_{v_{11}}^{ad}}{\partial R} \right\rangle}{(E_{v_{11}} - E_{v_{12}}^0) (E_{v_{11}} - E_{v_3}^0)}. \quad (19)$$

Harmonic oscillator wavefunctions have the property that

$$\frac{\partial}{\partial R} |\xi_v\rangle = -\sqrt{\frac{\omega\mu}{2\hbar}} \left[(v+1)^{1/2} |\xi_{v+1}\rangle - (v)^{1/2} |\xi_{v-1}\rangle \right], \quad (20)$$

i.e., that the derivative of the wavefunction of level v yields a linear combination of level $v+1$ and level $v-1$ wavefunctions. Thus we see that for slowly varying functions $\langle \Phi_{12}^{ad} \left| \frac{\partial}{\partial R} \right| \Phi_3^{ad} \rangle$ and $\langle \Phi_3^{ad} \left| \frac{\partial}{\partial R} \right| \Phi_{11}^{ad} \rangle$, there should be a strong interaction between levels satisfying $v_{11} = v_{12}$ and $v_{11} = v_{12} \pm 2$. [The first term in Eq. (13) would also lead to interaction between levels satisfying $v_{11} = v_{12}$.] The energy denominator $(E_{v_{11}} - E_{v_{12}}^0)$ in Eq. (19) strongly favors interaction between levels close in energy. For the $11(0^+)$ and $12(0^+)$ states, levels that are nearest neighbors satisfy $v_{11} = v_{12} + 2$. This argument suggests that we need only consider interactions of v_{11} with this one particular vibrational level of the $12(0^+)$ state $v_{12} = v_{11} - 2$, and write Eq. (14) as

$$|\Psi_1\rangle = a_1 \left| \xi_{v_{11}}^J \right\rangle |\Phi_{11}\rangle + b_1 \left| \xi_{v_{12}=v_{11}-2}^J \right\rangle |\Phi_{12}\rangle + \sum_{v_3} c_{1,v_3} \left| \xi_{v_3}^J \right\rangle |\Phi_3\rangle. \quad (21)$$

Making a similar argument for the mixed wavefunction of the level of predominantly $12(0^+)$ character, we can approximate Eq. (15) by

$$|\Psi_2\rangle = a_2 \left| \xi_{v_{11}=v_{12}+2}^J \right\rangle |\Phi_{11}\rangle + b_2 \left| \xi_{v_{12}}^J \right\rangle |\Phi_{12}\rangle + \sum_{v_3} c_{2,v_3} \left| \xi_{v_3}^J \right\rangle |\Phi_3\rangle. \quad (22)$$

The orthogonality of the rotational wavefunctions requires that only levels of the same value of J can interact.

Now to simulate the resolved fluorescence spectra that correspond to each of these levels, we first determine the Hund's case (a) singlet and triplet amplitudes of each upper level wavefunction, since the bound-free and bound-bound fluorescence, due to downward transitions to the lowest triplet

and singlet states, respectively, can be described in terms of Hund's case (a) wavefunctions and electric dipole selection rules. To do this, we insert Eqs. (5) and (6) into Eqs. (21) and (22) and rearrange terms to emphasize singlet and triplet components:

$$|\Psi_1\rangle = a_1 \left[\frac{b_1}{a_1} \cos \theta(R) \left| \xi_{v_{12}=v_{11}-2}^J \right\rangle - \sin \theta(R) \left| \xi_{v_{11}}^J \right\rangle \right] |\Phi_{7^1\Sigma^+}\rangle + a_1 \left[\cos \theta(R) \left| \xi_{v_{11}}^J \right\rangle + \frac{b_1}{a_1} \sin \theta \left| \xi_{v_{12}=v_{11}-2}^J \right\rangle \right] |\Phi_{5^3\Pi_{0^+}}\rangle + a_1 \sum_{v_3} \frac{c_{1,v_3}}{a_1} \left| \xi_{v_3}^J \right\rangle |\Phi_3\rangle \quad (23)$$

and

$$|\Psi_2\rangle = b_2 \left[\cos \theta(R) \left| \xi_{v_{12}}^J \right\rangle - \frac{a_2}{b_2} \sin \theta(R) \left| \xi_{v_{11}=v_{12}+2}^J \right\rangle \right] |\Phi_{7^1\Sigma^+}\rangle + b_2 \left[\sin \theta \left| \xi_{v_{12}}^J \right\rangle + \frac{a_2}{b_2} \cos \theta(R) \left| \xi_{v_{11}=v_{12}+2}^J \right\rangle \right] |\Phi_{5^3\Pi_{0^+}}\rangle + b_2 \sum_{v_3} \frac{c_{2,v_3}}{b_2} \left| \xi_{v_3}^J \right\rangle |\Phi_3\rangle. \quad (24)$$

In these expressions, it is convenient to use the non-relativistic electronic wavefunctions $|\Phi_{5^3\Pi_{0^+}}\rangle$ and $|\Phi_{7^1\Sigma^+}\rangle$ since it is then obvious which components of the wavefunction are responsible for the bound-free (triplet) emission and which are responsible for the bound-bound (singlet) emission. If we assume that the mixing coefficients (b_1/a_1) and (a_2/b_2) and the mixing angle, θ , are all small, the triplet emission associated with $|\Psi_1\rangle$ is dominated by the $\xi_{v_{11}}^J$ vibrational wavefunction. Similarly, the singlet emission associated with $|\Psi_2\rangle$ is dominated by the $\xi_{v_{12}}^J$ vibrational wavefunction. In this work, we refer to these components as the direct term components, because the $11(0^+)$ and $12(0^+)$ states are predominantly of triplet and singlet character, respectively. This is also why we assign the $12(0^+)$ state vibrational quantum numbers based on the resolved $12(0^+) \rightarrow 1(X)^1\Sigma^+$ bound-bound emission intensity pattern, rather than on the $12(0^+) \rightarrow 1(a)^3\Sigma^+$ bound-free intensity pattern.

However, again assuming the mixing coefficients, (b_1/a_1) and (a_2/b_2) , and the mixing angle, θ , are small, and that (b_1/a_1) , (a_2/b_2) , and $\tan \theta(R)$ are roughly comparable in magnitude, the singlet emission associated with $|\Psi_1\rangle$, and the triplet emission associated with $|\Psi_2\rangle$ are not dominated by either the $11(0^+)$ or the $12(0^+)$ vibrational wavefunction. We refer to these wavefunction components as cross term components. These cross term components show how the vibrational wavefunctions can mix together to produce an upper state wavefunction with unusual resolved fluorescence spectra. Both $\xi_{v_{11}}^J$ and $\xi_{v_{12}=v_{11}-2}^J$ vibrational wavefunctions contribute significantly to the sums

in the cross term components, such that the resolved fluorescence spectra exhibit quantum interference. It is essential to emphasize that *this interference requires two types of interaction* (in this case via spin-orbit and non-adiabatic mechanisms) between the interacting levels.

B. Resolved fluorescence from the 11(0⁺) and 12(0⁺) states

In order to test the model described by Eqs. (23) and (24), we simulated resolved fluorescence spectra for 11(0⁺), 12(0⁺) \rightarrow 1(X)¹ Σ^+ , 1(a)³ Σ^+ transitions. This was done for three pairs of 11(0⁺) (v_{11} , J) and 12(0⁺) (v_{12} , J) levels. The specific levels were chosen because their emission spectra are relatively strong with good signal-to-noise, and the intensity patterns in the parts of the spectra associated with the cross terms are specific to a particular level and yet still fairly simple.

We start by defining a parameter K ,

$$K \equiv \frac{(a_2/b_2)}{\tan \theta}, \quad (25)$$

which allows us to rewrite Eq. (24) as

$$|\Psi_2\rangle = D \left\{ \left[\cot \theta |\xi_{v_{12}}^J\rangle - K \tan \theta |\xi_{v_{11}=v_{12}+2}^J\rangle \right] |\Phi_{7^1\Sigma^+}\rangle + \left[|\xi_{v_{12}}^J\rangle + K |\xi_{v_{11}=v_{12}+2}^J\rangle \right] |\Phi_{5^3\Pi_0^+}\rangle + \frac{1}{\sin \theta} \sum_{v_3} \frac{c_{2,v_3}}{b_2} |\xi_{v_3}^J\rangle |\Phi_3\rangle \right\}, \quad (26)$$

where $D = b_2 \sin \theta$.

Thus K is a measure of the relative $\xi_{v_{11}=v_{12}+2}^J$ and $\xi_{v_{12}}^J$ vibrational wavefunction amplitudes in the cross term [$\Phi_{5^3\Pi_0^+}$ term] component of $|\Psi_2\rangle$.

To simulate the spectra, we first applied the model to vibrational levels that are nearest neighbors in terms of energy and that also satisfy $v_{11} = v_{12} + 2$. Figure 5 shows one example of this type of mixing of vibrational wavefunctions. We used the computer programs LEVEL⁷² and a modified version of BCONT^{75,76} to carry out the simulations. First, level energies and vibrational wavefunctions were calculated with LEVEL using experimental 11(0⁺) and 12(0⁺) potentials for the ro-vibrational levels of interest. In these calculations, the IPA potential of the present work (Table II) was used for the 12(0⁺) state and the experimental IPA potential from Ref. 52 was used for the 11(0⁺) state. Direct and cross term components were constructed using the wavefunctions

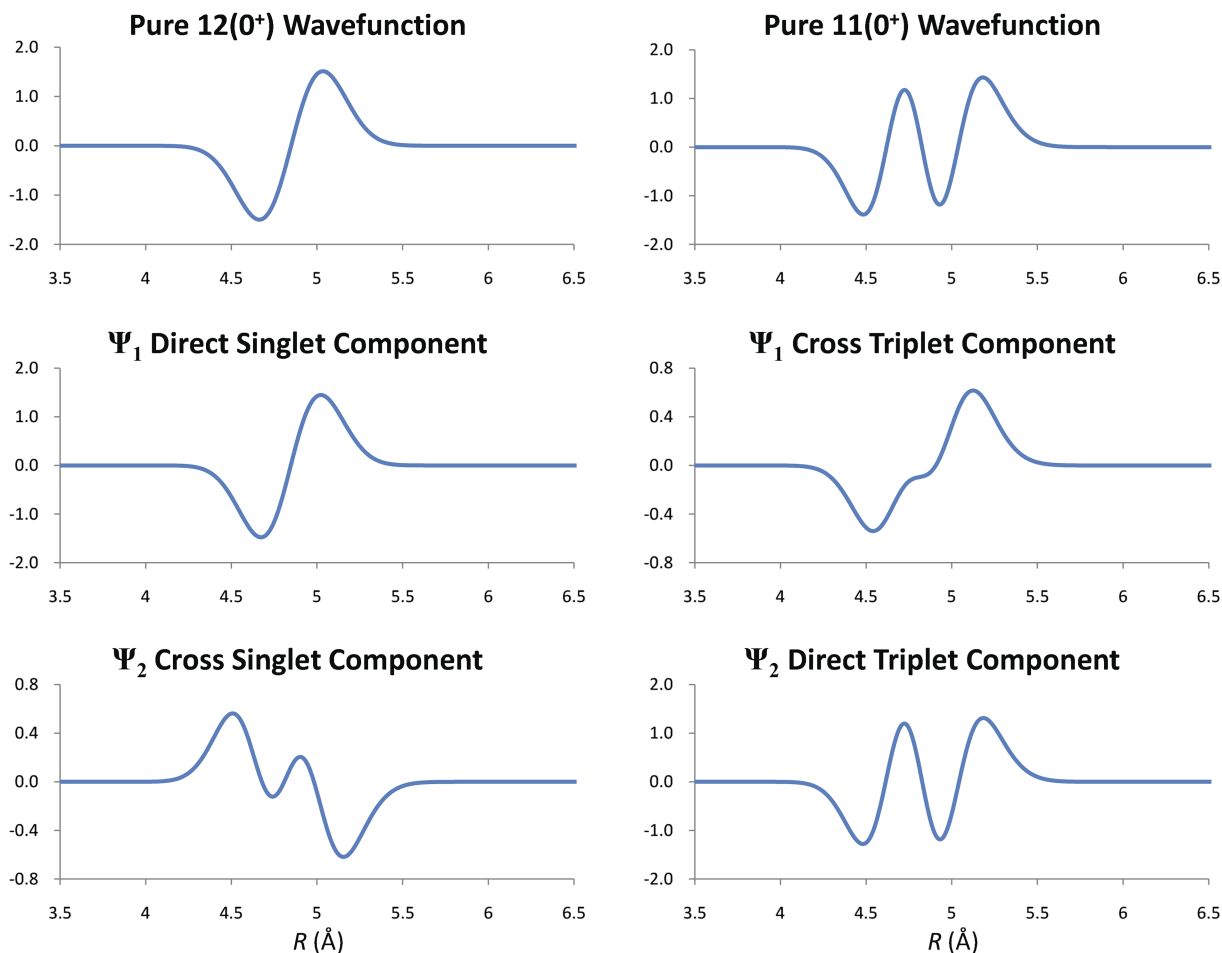


FIG. 5. Pure and mixed vibrational wavefunctions vs. internuclear separation (Å) for particular levels of the NaCs 11(0⁺) and 12(0⁺) states. The top row shows plots of pure wavefunctions for the 12(0⁺)(1, 43) and 11(0⁺)(3, 43) levels (left and right, respectively), calculated using the computer program LEVEL.⁷² The second row shows the singlet and triplet wavefunction components for the state Ψ_1 described by Eq. (23). The third row shows the singlet and triplet wavefunction components for the state Ψ_2 described by Eq. (24). These mixed wavefunction components were calculated using $(b_1/a_1) = -0.195$, $(a_2/b_2) = 0.2116$, and $\theta = 0.311$ rad.

calculated from these potentials and selected values of (b_1/a_1) , (a_2/b_2) , and θ according to Eqs. (23) and (24).

In this first “proof of principle” calculation of these mixed wavefunctions, we took the mixing angle θ to be independent of internuclear separation; i.e., $\theta(R) = \theta_{\text{ave}}$. This approximation is discussed in Sec. IV C where we use the experimental potentials to carry out an approximate calculation of $\theta(R)$. Once an appropriate set of mixing parameters was chosen, the vibrational wavefunction components (23) and (24) were input to BCONT in order to simulate the spectra from these mixed levels. Using an independently specified wavefunction in BCONT allows the user to bypass the input of an initial upper state potential. Rather than BCONT calculating the level energy and wavefunction of the selected upper state level, a separate input file for the modified BCONT^{76,77} provides the level energy and point-wise wavefunction. The calculated spectra were compared to experimental spectra in three stages, in order to fit the amplitude ratios, (b_1/a_1) and (a_2/b_2) , and the mixing angle θ .

As can be seen from Eq. (26), the value of K determines the intensity distribution in the part of the spectrum that results from the cross term [$\Phi_{5^3\Pi_{0^+}}$ term] component of $|\Psi_2\rangle$. Therefore, we first varied K until the simulated triplet part of the $12(0^+)$ spectrum, corresponding to the triplet cross term component, matched the experimental spectrum as closely as possible in a least squares sense. The overall normalization factor D was used to scale the simulations to ensure that the integrated areas of the experimental and simulated spectra were equal. The scaled simulation was compared to the experimental spectrum at each point along the wavelength grid used in the BCONT calculation, and the RMS deviation was determined. The value of K was adjusted iteratively. After each simulation, K was adjusted to obtain new cross term wavefunction components that were input to BCONT for the next iteration of the simulation. We varied K until the RMS deviation was minimized for the bound-free fluorescence associated with

each of the three $12(0^+)$ ro-vibrational levels studied. Figures 6(b), 7(b), and 8(b) show the bound-free (triplet) parts of the simulated spectra associated with each optimized cross term component in Eq. (26) along with the experimental spectra associated with the corresponding $12(0^+) \rightarrow 1(a)^3\Sigma^+$ transitions. In these simulations, the relative $5^3\Pi_{0^+} \rightarrow 1(a)^3\Sigma^+$ transition dipole moment function determined in Ref. 52 was used, along with the experimental $1(a)^3\Sigma^+$ potential curve reported in Refs. 52 and 44.

Once the intensity distribution of the $12(0^+)$ triplet spectra associated with the cross term components was reproduced as closely as possible, we began the second stage of fitting. This involved varying (a_2/b_2) (with θ adjusted so that the value of K remained fixed) in order to best reproduce the relative total intensities of the singlet and triplet components for the level with predominantly $12(0^+)$ character in each pair of mixed levels. From Eq. (24), we can see that, for small values of θ and (a_2/b_2) , an increase in θ and (a_2/b_2) (keeping K fixed) will result in little change to the overall magnitudes of the direct component [$\Phi_{7^1\Sigma^+}$ term], but will cause the overall relative magnitude of the cross component [$\Phi_{5^3\Pi_{0^+}}$ term] to increase significantly. Thus, a larger value of (a_2/b_2) results in a larger triplet intensity relative to the singlet emission.

The relative singlet and triplet emission from a particular level is also heavily influenced by the transition dipole moment functions. For the triplet emission from both the $11(0^+)$ and $12(0^+)$ states, we used the experimental relative $5^3\Pi_{0^+} \rightarrow 1(a)^3\Sigma^+$ transition dipole moment function from Ref. 52, normalized to the theoretical transition dipole moment of Ref. 56. For the singlet emission from both states, the theoretical $7^1\Sigma^+ \rightarrow 1(X)^1\Sigma^+$ transition dipole moment function from Ref. 56 was used. The observed ratio of singlet emission intensity to triplet emission intensity for a particular experimental spectrum is also affected by the efficiency of the detection system as a function of wavelength. Therefore all spectra used for

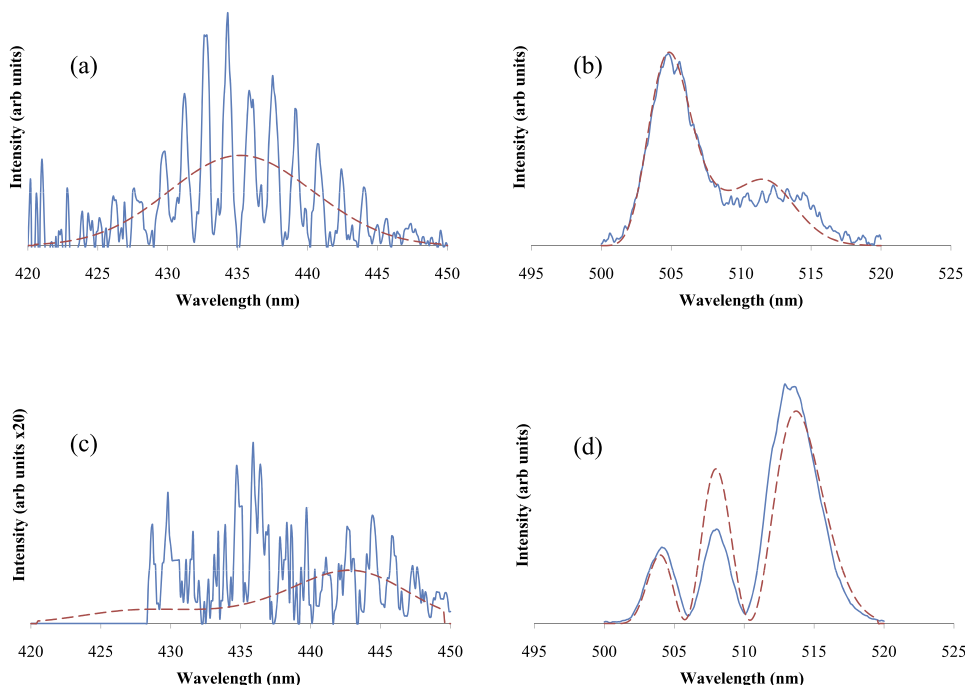


FIG. 6. Comparison of experimental (solid—blue) and simulated (dashed—red) spectra for (a) $12(0^+)$ (0, 43) $\rightarrow 1(X)^1\Sigma^+$, (b) $12(0^+)$ (0, 43) $\rightarrow 1(a)^3\Sigma^+$, (c) $11(0^+)$ (2, 43) $\rightarrow 1(X)^1\Sigma^+$, and (d) $11(0^+)$ (2, 43) $\rightarrow 1(a)^3\Sigma^+$ transitions. The intensity distributions result from mixing pure $11(0^+)$ (2, 43) and $12(0^+)$ (0, 43) vibrational wavefunctions according to Eqs. (23) and (24) with $(b_1/a_1) = -0.486 \pm 0.002$, $(a_2/b_2) = 0.1032 \pm 0.0008$, and $\theta = 0.248 \pm 0.007$ radians.

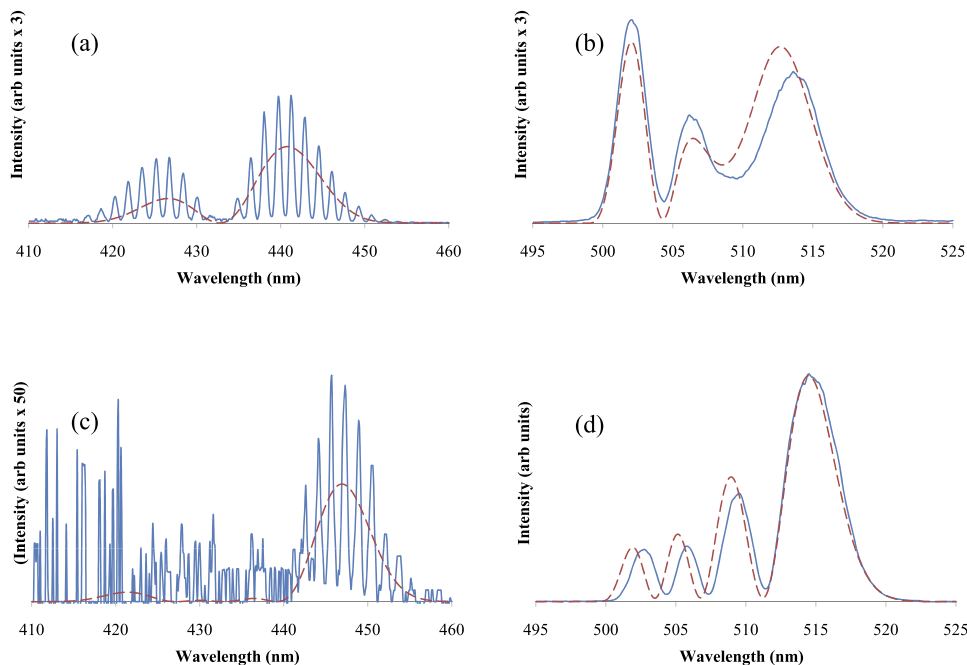


FIG. 7. Comparison of experimental (solid—blue) and simulated (dashed—red) spectra for (a) $12(0^+)$ (1, 43) $\rightarrow 1(X)^1\Sigma^+$, (b) $12(0^+)$ (1, 43) $\rightarrow 1(a)^3\Sigma^+$, (c) $11(0^+)$ (3, 43) $\rightarrow 1(X)^1\Sigma^+$, and (d) $11(0^+)$ (3, 43) $\rightarrow 1(a)^3\Sigma^+$ transitions. The intensity distributions result from mixing pure $11(0^+)$ (3, 43) and $12(0^+)$ (1, 43) vibrational wavefunctions according to Eqs. (23) and (24) with $(b_1/a_1) = -0.195 \pm 0.001$, $(a_2/b_2) = 0.2116 \pm 0.0001$, and $\theta = 0.311 \pm 0.002$ radians.

fitting (and plotted in the various figures here) were first corrected for the detection efficiency. Finally, we used the version of BCONT modified by McGeehan *et al.*⁷⁶ to simulate both the singlet and triplet emission for both states, even though the singlet emission is bound-bound. This version simulates bound-bound transitions as a continuum by treating the discrete levels as a continuum described by a density of states. The modified version of BCONT also correctly treats the relative intensities of bound-free and bound-bound emission (see Ref. 76). Normalization is preserved in these calculations, so the experimental and simulated spectra were compared using total integrated areas.

For a given $12(0^+)$ ro-vibrational level, a value of (a_2/b_2) was chosen and the value of θ was calculated from

$$\theta = \tan^{-1} \left[\frac{(a_2/b_2)}{K} \right]. \quad (27)$$

The various components of the vibrational wavefunctions in Eq. (24) were calculated and input to BCONT. The simulated triplet spectrum for each level was scaled to match the total integrated intensity of the corresponding experimental triplet spectrum. The simulated (quasi-continuum) singlet emission spectrum for each level was then scaled by the same factor used for the triplet emission associated with that level. Next, the ratio of the total integrated areas of the singlet to triplet emission was calculated for the experimental and simulated spectra for both levels. Finally, (a_2/b_2) was varied until the RMS difference between

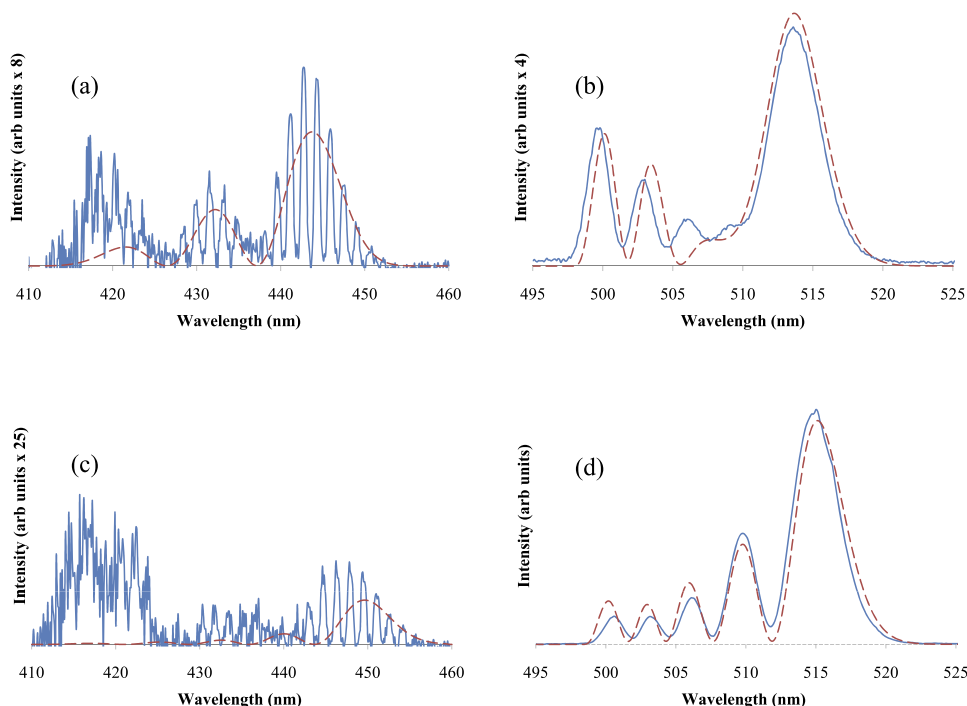


FIG. 8. Comparison of experimental (solid—blue) and simulated (dashed—red) spectra for (a) $12(0^+)$ (2, 33) $\rightarrow 1(X)^1\Sigma^+$, (b) $12(0^+)$ (2, 33) $\rightarrow 1(a)^3\Sigma^+$, (c) $11(0^+)$ (4, 33) $\rightarrow 1(X)^1\Sigma^+$, and (d) $11(0^+)$ (4, 33) $\rightarrow 1(a)^3\Sigma^+$ transitions. The intensity distributions result from mixing pure $11(0^+)$ (4, 33) and $12(0^+)$ (2, 33) vibrational wavefunctions according to Eqs. (23) and (24) with $(b_1/a_1) = -0.0472 \pm 0.0001$, $(a_2/b_2) = 0.2878 \pm 0.0001$, and $\theta = 0.328 \pm 0.003$ radians.

these simulated and experimental integrated intensity ratios for the two levels was minimized. This completed the simulations of the singlet and triplet emission associated with the $12(0^+)$ level of each pair [parts (a) and (b) of Figs. 6, 7, and 8].

In the third stage of fitting, we fixed θ to the final value obtained from the $12(0^+)$ singlet and triplet spectra [Eq. (27)], using the best fit values for (a_2/b_2) and K , and varied the amplitude ratio (b_1/a_1) in Eq. (23) to reproduce the relative singlet and triplet emission intensities from the predominantly $11(0^+)$ level of each mixed pair of levels [parts (c) and (d) of Figs. 6, 7, and 8]. The values of (b_1/a_1) and θ also affect the intensity distribution of the singlet cross term component [the $\Phi_{7^1\Sigma^+}$ term in Eq. (23)]. Therefore, it should, in principle, be possible to use the intensity distributions associated with both cross term components to obtain the best value for θ . Despite this, we used the intensity distribution of the $12(0^+) \rightarrow 1(a)^3\Sigma^+$ spectra alone to obtain K and hence θ , because the $11(0^+) \rightarrow 1(X)^1\Sigma^+$ spectra are very weak and noisy in comparison.

Table III lists the best fit parameters for each pair of levels studied here. Figures 6, 7, and 8 show comparisons of the experimental and simulated spectra obtained from these fits for each pair of interacting levels. Note that the signal-to-noise ratio is quite low on the short wavelength end of several of the singlet spectra because the detector efficiency in the violet range is poor. The detector efficiency is about $22\times$ greater in the green spectral region associated with the bound-free emission than in the violet region, and just within the violet region it decreases by a factor of six between 450 nm and 420 nm (see Ref. 78). The signal-to-noise at the short wavelength end of the singlet emission [especially for emission originating in $11(0^+)$ levels] is further reduced by the relatively small $7^1\Sigma^+ \rightarrow 1(X)^1\Sigma^+$ transition dipole moment.⁵⁶

C. Discussion of assumptions and approximations used in the model

The model described in Sec. IV A requires two separate types of interaction to reproduce the experimental spectra. We assume that the first mechanism is due to the spin-orbit interaction, since both electronic states involved in the mixing are observed to radiate to lower triplet states and to lower singlet states.

In writing Eqs. (5) and (6), we have assumed that the spin-orbit interaction only mixes the electronic non-relativistic wavefunctions of two electronic states. This neglects spin-orbit interactions of the $11(0^+)$ [$5^3\Pi_{0^+}$] and $12(0^+)$ [$7^1\Sigma^+$] states with other nearby states such as $10(0^+)$, $13(0^+)$, and $14(0^+)$. Although spin-orbit interactions between these states and the

$11(0^+)$ and $12(0^+)$ states are certainly possible, the energy gaps are much larger than the gap between $11(0^+)$ and $12(0^+)$. Thus we concluded a two-state model for the spin-orbit interaction is appropriate.

In simulations based on our simplified model, we have taken the spin-orbit mixing angle, θ , as constant, despite the fact that Eqs. (5) and (6) allow for an R dependence of the relativistic electronic wavefunctions through the mixing angle $\theta(R)$. In Subsection 2 of the Appendix [Eq. (A21)], we show that the off-diagonal spin-orbit Hamiltonian matrix element can be determined from the mixing angle θ and the splitting of the perturbed (i.e., relativistic, spin-orbit included) electronic states:

$$|H_{SO}| = \frac{1}{2} \sin 2\theta \left(E_{12(0^+)} - E_{11(0^+)} \right). \quad (28)$$

Here $H_{SO} = \langle \Phi_{5^3\Pi_{0^+}}(\vec{r}, R) | \hat{H}_{SO} | \Phi_{7^1\Sigma^+}(\vec{r}, R) \rangle$ is the spin-orbit Hamiltonian matrix element between the non-relativistic $5^3\Pi_{0^+}$ and $7^1\Sigma^+$ electronic states. The average splitting of the $12(0^+)$ and $11(0^+)$ electronic states over the range of R ($\sim 4-6$ Å) that is relevant to the states we use in our fitting is approximately 126 cm^{-1} , based on the experimental potentials [see Fig. 9(a)]. From our fitting process described above, we find levels that correspond to this range of R have an average θ of 0.296 radians. This gives us an estimate of the electronic spin-orbit interaction constant, $|H_{SO}| = 35.1 \text{ cm}^{-1}$.

Now if we assume H_{SO} is constant, we can use this estimated value to determine the approximate R dependence of the function $\theta(R)$. From Eq. (A22),

$$\theta(R) = \frac{1}{2} \sin^{-1} \left(\frac{2|H_{SO}|}{[E_{12(0^+)}(R) - E_{11(0^+)}(R)]} \right). \quad (29)$$

Using the experimental $11(0^+)$ and $12(0^+)$ potentials, we obtain the $\theta(R)$ function plotted in Fig. 9(b). From this plot, we see that $\theta(R)$ is fairly constant over the range $4 \text{ Å} \leq R \leq 5.8 \text{ Å}$. At $R > 5.88 \text{ Å}$ we find $2|H_{SO}| > E_{12(0^+)}(R) - E_{11(0^+)}(R)$, so the inverse sine function is not defined. This breakdown is probably related to the fact that H_{SO} very likely has some R dependence. The experimental $12(0^+)$ potential has only been determined in the range 4-5.96 Å, so the fact that the experimental $11(0^+)$ and $12(0^+)$ potentials appear to cross just above 6.16 Å [Fig. 9(a)] is not to be believed.

We believe this analysis justifies the treatment of the spin-orbit interaction in our model [i.e., Eqs. (5) and (6)]. Specifically, the values of θ obtained from our fits seem plausible in light of the expected magnitude of the spin-orbit interaction. We think it also justifies taking $\theta(R)$ to be independent of R , at least as a first approximation.

TABLE III. Fitted parameters $(a_2/b_2, b_1/a_1, \text{ and } \theta)$ for the mixed level vibrational wavefunctions Eqs. (23) and (24) and K defined in (25). The uncertainties given for each parameter represent statistical (one σ) uncertainties only.

v_{11}	v_{12}	J	K	a_2/b_2	b_1/a_1	θ (rad)
0	2	43	0.408 ± 0.009	0.1032 ± 0.0008	-0.486 ± 0.002	0.248 ± 0.007
1	3	43	0.659 ± 0.004	0.2116 ± 0.0001	-0.195 ± 0.001	0.311 ± 0.002
2	4	33	0.845 ± 0.009	0.2878 ± 0.0001	-0.0472 ± 0.0001	0.328 ± 0.003

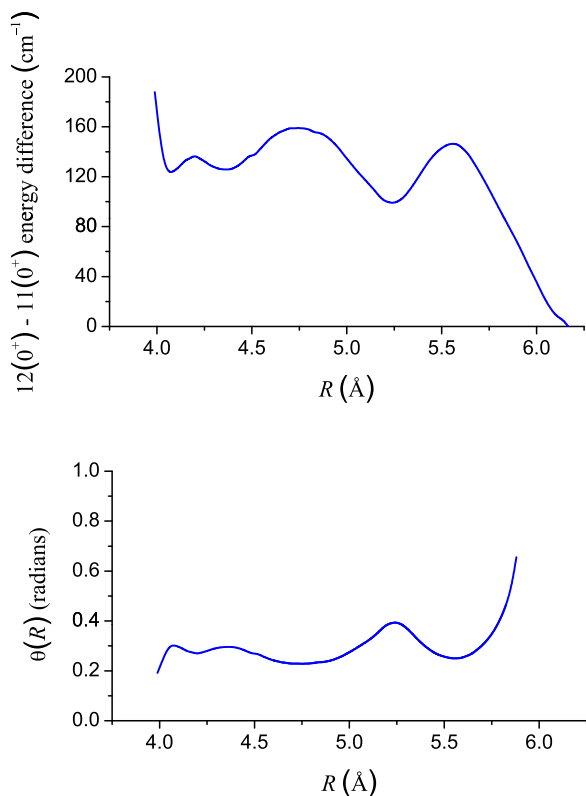


FIG. 9. (a) Difference in energy of the NaCs $12(0^+)$ and $11(0^+)$ experimental electronic potentials (from this work and Ref. 52, respectively), as a function of internuclear separation R . (b) Mixing angle $\theta(R)$ describing the spin-orbit interaction between the $7^1\Sigma^+$ and $5^3\Pi_{0^+}$ electronic states [see Eq. (29)].

In addition, $\theta(R)$ is a global parameter that is only weakly dependent on the specific *vibrational* levels of the two states (through the different ranges of R spanned by the different vibrational wavefunctions). Therefore, especially in this lowest-order approximation, where $\theta(R)$ is taken to be independent of R , consistency should probably require that the same value of θ be used for all three simulations shown in Figs. 6–8. Instead, as Table III indicates, we obtained three slightly different best fit values $\theta = 0.248, 0.311,$ and 0.328 for the three simulations we carried out.

However, a significant dependence of θ on R would clearly influence the average value of θ for a particular pair of interacting levels as well as the magnitude of the interference in the cross terms of the mixed wavefunctions. As seen in Fig. 9(a), the $11(0^+)$ and $12(0^+)$ potential curves are nearly parallel, so the assumption of a constant value of H_{SO} results in a nearly constant $\theta(R)$ function [as plotted in Fig. 9(b)]. However, Salami *et al.*⁷⁹ and Harker *et al.*⁸⁰ have used Morse functions to describe empirical and *ab initio* spin-orbit functions, H_{SO} , for Rb_2 and NaK , respectively. So a significant R dependence to θ is entirely possible, despite the relative flatness of the $\theta(R)$ curve in Fig. 9(b).

Although we did not include any R dependence in our fitting of θ , the agreement between the simulations and the experimental spectra is fairly good, and remaining systematic discrepancies can likely be attributed to its neglect. Because the emission resulting from the cross term components of the mixed wavefunctions is very sensitive to θ , it is possible that a more complicated fit could do a better job of determining the

general dependence of θ on R . As an example, Fig. 10 shows a simulation of the triplet emission from the $12(0^+)$ (1, 43) level, where θ is assumed to have a simple linear dependence on R ,

$$\theta(R) = \theta_{\text{ave}} + m(R - R_0), \quad (30)$$

and θ_{ave} is the average value of θ as determined in the fit that produced the simulation shown in Fig. 7(b), m is the fit parameter that describes the slope, and $R_0 = 4.8745 \text{ \AA}$. The best fit value is given by $m = 0.18 \pm 0.01 \text{ \AA}^{-1}$. Comparison of Figs. 7(b) and 10 indicates that the linear $\theta(R)$ function provides a somewhat better fit (χ^2 reduced by about one half) to the experimental spectrum than $\theta = \text{constant}$. It also appears likely that inclusion of a quadratic term in $\theta(R)$ would give even better agreement. Such a quadratic term might also explain why the best fit θ_{ave} values increase slightly with increasing vibrational levels, since higher vibrational levels span ranges of R that include both larger and smaller values than are sampled by lower vibrational levels. Further investigation of this R dependence of θ is planned for the future.

As we have argued previously, the second interaction between specific vibrational levels v_{11} and $v_{12} = v_{11} - 2$ of the $11(0^+)$ and $12(0^+)$ electronic states is most likely due to a second-order non-adiabatic interaction via a third state (labeled state 3 above). These interactions are due to terms that involve derivatives with respect to the internuclear separation, R , which are generally neglected when the Born-Oppenheimer approximation is invoked.⁷ As explained above, we believe there is no first-order interaction between the $11(0^+)$ and $12(0^+)$ states, due to this mechanism, but such interactions can occur in second-order through another electronic state, such as $10(0^+)$ or $13(0^+)$. From Eqs. (19) and (20), we see that the term that connects v_{11} and $v_{12} = v_{11} - 2$ can be written as

$$\frac{b_{1,v_{12}}}{a_1} \approx -\frac{\hbar^3}{2\mu} \sqrt{\omega_{e,11}\omega_{e,12}} (v_{12} + 1)^{1/2} (v_{11})^{1/2} \times \frac{\langle \xi_{v_{12}+1}^{ad} | \langle \Phi_{12}^{ad} | \frac{\partial}{\partial R} | \Phi_3^{ad} \rangle \langle \Phi_3^{ad} | \frac{\partial}{\partial R} | \Phi_{11}^{ad} \rangle | \xi_{v_{11}-1}^{ad} \rangle}{(E_{v_{11}} - E_{v_{12}}^0) (E_{v_{11}} - E_{v_3}^0)}. \quad (31)$$

For two adiabatic states that undergo an avoided crossing at $R = R_c$ (i.e., at the point where the diabatic states cross), we can

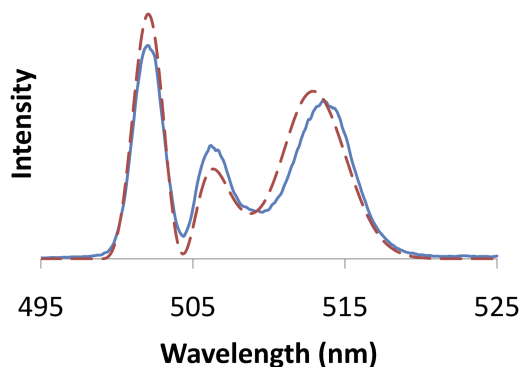


FIG. 10. Simulated $12(0^+)$ (1, 43) $\rightarrow 1(a)^3\Sigma^+$ emission calculated using a linear R -dependence for θ [Eq. (30)], with $\theta_{\text{ave}} = 0.311$ radians, $R_0 = 4.8745 \text{ \AA}$, and $m = 0.18 \pm 0.01 \text{ \AA}^{-1}$. The reduced χ^2 value here is 4.96, compared to 10.84 for the same fit with θ independent of R .

use Eq. (3.3.14) of Ref. 7, to estimate the maximum values of the electronic matrix elements:

$$\langle \Phi_{11,12}^{ad} | \frac{\partial}{\partial R} | \Phi_3^{ad} \rangle \approx \frac{E_{11,12}^d(R) - E_3^d(R)}{4H^e(R - R_c)}, \quad (32)$$

where H^e represents half the vertical energy difference between the adiabatic $11(0^+)$ or $12(0^+)$ state and the adiabatic state 3 at the location of the avoided crossing, and $E_{11,12}^d(R) - E_3^d(R)$ is the vertical separation of the diabatic states at an R value near to but not equal to R_c (i.e., using a linear model of the curve crossing). If state 3 is the $10(0^+)$ state, we can use the theoretical potentials⁵⁵ to estimate $\langle \Phi_{11,12}^{ad} | \frac{\partial}{\partial R} | \Phi_3^{ad} \rangle \approx 0.7 \text{ \AA}^{-1}$. Then from Eq. (31), we estimate that $b_1/a_1 \approx 0.002$ (and similarly for a_2/b_2). This value is too small to explain our fitted values, but the estimate is strongly dependent on details of the state 3 electronic energy function. According to the theoretical calculations,⁵⁵ there is an avoided crossing at $R \sim 5.5 \text{ \AA}$ between the $13(0^+)$ and $14(0^+)$ potentials, which represents an interaction between the $8^1\Sigma^+$ and $6^3\Pi$ diabatic states. Details of this interaction may be important for the non-adiabatic interaction of the $13(0^+)$ state with the $11(0^+)$ and $12(0^+)$ states. The $13(0^+)$ and $14(0^+)$ states are the highest states of 0^+ symmetry in the theoretical calculations, and therefore, their computed properties are expected to be less accurate than those for states lying lower in energy. We note that because b_1/a_1 and a_2/b_2 depend on R only through integrals over R in the Hamiltonian matrix elements, the fitting parameters b_1/a_1 and a_2/b_2 are independent of R .

Our experimental results support the idea that the two vibrational levels v_{11} and v_{12} interact with one another only if the vibrational quantum numbers are related by $v_{11} = v_{12} + 2$. The model presented above identifies the second interaction as a non-adiabatic interaction via a third state, and if this model is substantially correct, there is also a possibility for interaction of levels obeying $v_{11} = v_{12}$ and $v_{11} = v_{12} - 2$. However, for the low-lying vibrational levels, level $v_{11} = v_{12} + 2$ generally lies closest in energy to level v_{12} with an average separation of about 20 cm^{-1} , while levels $v_{11} = v_{12}$ and $v_{11} = v_{12} - 2$ are separated from level v_{12} by $\sim 140 \text{ cm}^{-1}$ and $\sim 245 \text{ cm}^{-1}$, respectively. Thus, we believe the mixing of v_{12} with levels obeying $v_{11} = v_{12}$ and $v_{11} = v_{12} - 2$ is suppressed by the much larger energy separations. However, for most low-lying vibrational levels, v_{12} and $v_{11} = v_{12} + 3$ do not have much larger energy separations than the nearest-neighbor pairs v_{12} and $v_{11} = v_{12} + 2$ (i.e., the separations of v_{12} and $v_{11} = v_{12} + 3$ are typically $\sim 30 \text{ cm}^{-1}$ compared to $\sim 20 \text{ cm}^{-1}$ for v_{12} and $v_{11} = v_{12} + 2$). Although many types of interactions are strongest for nearest neighbor pairs, we believe the major argument supporting the validity of the model we propose here is that it explains the observation that only levels v_{12} and $v_{11} = v_{12} + 2$ appear to interact, and that other pairs, with only slightly larger energy separations (such as v_{12} and $v_{11} = v_{12} + 3$), do not appear to interact. Specifically, we find that simulations based on mixed levels built from nearest neighbor pairs (v_{12} and $v_{11} = v_{12} + 2$) yield the best agreement with experimental spectra. We have also carried out simulations using next nearest neighbor pairs (v_{12} and $v_{11} = v_{12} + 3$). Figure 2 of the [supplementary material](#) shows the best fit result from a set of simulations

based on mixtures of $12(0^+)$ (1, 43) and $11(0^+)$ (4, 43) wavefunctions. From that figure, it is evident that the agreement with the experimental spectrum is poor. It is also clear that there cannot be any significant mixing of v_{12} with higher vibrational levels of the $11(0^+)$ state since wavefunctions for such levels span a larger range of R and hence should produce emission at longer wavelengths than observed in the experimental spectra. Finally, in Fig. 3 of the [supplementary material](#), we show the best fit result from a set of simulations based on mixtures of $12(0^+)$ (1, 43) and $11(0^+)$ (2, 43) wavefunctions, where it is evident that the agreement is also poor. Thus, we conclude that mixing with vibrational levels other than the nearest neighbor (v_{12} and $v_{11} = v_{12} + 2$) pairs is negligible.

Although Eqs. (23) and (24) suggest that admixtures of state 3 vibrational wavefunctions should also contribute to the emission associated with the predominantly $11(0^+)$ and $12(0^+)$ energy levels, we suspect that these contributions would tend to wash out because a number of state 3 vibrational wavefunctions would likely contribute and because these contributions would also likely be shifted in wavelength. We have observed emission from many $10(0^+)$ [$4^3\Pi_{0^+}$] levels, and the intensity distribution of the $4^3\Pi_{0^+} \rightarrow 1(a)^3\Sigma^+$ bound-free emission is quite different from that of the $11(0^+) \rightarrow 1(a)^3\Sigma^+$ or $12(0^+) \rightarrow 1(a)^3\Sigma^+$ emission reported here.

V. CONCLUSIONS

We measured 214 level energies for the $12(0^+)$ electronic state of NaCs using OODR spectroscopy. These energies were used to map out an experimental potential energy curve using the IPA method. The resulting potential curve reproduces the measured level energies with an RMS deviation of 0.034 cm^{-1} . The $12(0^+)$ electronic potential curve has a minimum that lies very close in energy to the minimum of the previously mapped $11(0^+)$ electronic state.⁵² Therefore, because the states are close in energy, it is likely that the two states interact with each other in some way.

In order to identify the electronic state excited during a scan of the probe laser frequency, many resolved fluorescence spectra were observed for both the $12(0^+)$ electronic state and the previously mapped $11(0^+)$ state. Since the intensity distributions of the bound-bound and bound-free fluorescence spectra from these states cannot be explained by non-interacting electronic states, we proposed an interaction model that involves two separate interactions for the $11(0^+)$ and $12(0^+)$ states. The electronic states interact directly via the spin-orbit interaction, characterized by the mixing parameter $\theta(R)$. Individual ro-vibrational levels of these two electronic states can then also interact via a second mechanism, which we believe to be a second-order non-adiabatic interaction through a third (as yet unidentified) electronic state that we call state 3. Using the programs LEVEL⁷² and a modified version of BCONT,^{75,76} we were able to adjust the mixing angle, θ , and the mixing amplitude ratios, (b_1/a_1) and (a_2/b_2), in order to simulate bound-bound and bound-free fluorescence spectra that best reproduce our experimental spectra for three such pairs of interacting levels.

This interaction model allows us to estimate the electronic spin-orbit interaction constant, $|H_{SO}|$, and the R dependence

of the spin-orbit mixing angle $\theta(R)$. The model also does a fairly good job of reproducing experimental spectra, especially those portions of the spectra associated with cross term wavefunction components, such as the bound-free portions of the $12(0^+)$ resolved spectra. In addition, the model provides an explanation of the fact that vibrational levels v_{11} and v_{12} only seem to interact with one another if the vibrational quantum numbers are related by $v_{11} = v_{12} + 2$. Future work will continue to investigate the R -dependence of the θ parameter, and hence to determine the R dependence of the spin-orbit Hamiltonian matrix element between the non-relativistic $5^3\Pi_{0^+}$ and $7^1\Sigma^+$ electronic states, $H_{SO} = \langle \Phi_{5^3\Pi_{0^+}}(\vec{r}, R) | \hat{H}_{SO} | \Phi_{7^1\Sigma^+}(\vec{r}, R) \rangle$. Additional work will also try to reconcile the magnitude of the fitted amplitudes (b_1/a_1) and (a_2/b_2) with the much smaller calculated values based on our present knowledge of other NaCs electronic states that might play the role of state 3 in our model. Once theoretical potentials extending to higher energies become available, it may be possible to explain the magnitudes of the non-adiabatic interactions between the $13(0^+)$ state and the $11(0^+)$ and $12(0^+)$ states, respectively, that appear to be necessary to explain the current experimental results.

SUPPLEMENTARY MATERIAL

See the [supplementary material](#) for three figures and four tables in a single pdf file that has been placed on deposit. Figure 1 presents differences of experimental level energies and energies calculated with the best fit IPA potential. Figure 2 presents a comparison of experimental and simulated $12(0^+)$ (1, 43) $\rightarrow 1(a)^3\Sigma^+$ triplet emission calculated using a mixture of wavefunctions from the next nearest neighbor pair of levels $12(0^+)$ (1, 43) and $11(0^+)$ (4, 43). Figure 3 presents a comparison of experimental and simulated $12(0^+)$ (1, 43) $\rightarrow 1(a)^3\Sigma^+$ triplet emission calculated using a mixture of pure $12(0^+)$ (1, 43) and $11(0^+)$ (2, 43) wavefunctions. Table I provides a listing of NaCs $2(A)^1\Sigma^+(v_A, J') \leftarrow 1(X)^1\Sigma^+(v'', J'' = J' \pm 1)$ transitions used in this work. Table II lists the NaCs $12(0^+)$ (v, J) levels studied in this work. Ground state, intermediate state, and upper [$12(0^+)$] state levels and PUMP and PROBE laser frequencies are given for each transition studied in this work. Tables III and IV present the NaCs $12(0^+)$ RKR turning points and the IPA potential energy function, respectively. The tables have also been provided in MS Word format.

ACKNOWLEDGMENTS

This work was supported by the National Science Foundation under Grant Nos. PHY-0968898 and PHY-1403060 at

Lehigh University. R. W. Field thanks the US National Science Foundation [Grant No. CHE-1361865] for support of his research, which includes substantive collaborations. We are grateful to Professor Peet Hickman for useful discussions and to Dr. Kara Richter for assistance in the lab.

APPENDIX: USEFUL RESULTS FROM PERTURBATION THEORY

The following sections discuss aspects of perturbation theory and provide two useful results that are generally not found in the standard treatments.

1. Second order perturbation theory

In non-degenerate perturbation theory, we write the Hamiltonian as a sum of two terms

$$\hat{H} = \hat{H}^0 + \hat{H}', \quad (\text{A1})$$

where the first (zeroth order) term \hat{H}^0 has eigenfunctions ψ_i^0 and eigenvalues E_i^0 ; i.e.,

$$\hat{H}^0 \psi_i^0 = E_i^0 \psi_i^0. \quad (\text{A2})$$

The full Schrödinger equation can be written as

$$(\hat{H}_0 + \hat{H}') |\psi_i\rangle = E_i |\psi_i\rangle \quad (\text{A3})$$

and we wish to find the actual (perturbed) eigenfunctions ψ_i in terms of the unperturbed eigenfunctions. From (A3), we write

$$\begin{aligned} \langle \psi_i^0 | (\hat{H}_0 + \hat{H}') |\psi_i\rangle &= E_i \langle \psi_i^0 | \psi_i\rangle \\ E_i^0 \langle \psi_i^0 | \psi_i\rangle + \langle \psi_i^0 | \hat{H}' | \psi_i\rangle &= E_i \langle \psi_i^0 | \psi_i\rangle \\ \langle \psi_i^0 | \psi_i\rangle &= \frac{\langle \psi_i^0 | \hat{H}' | \psi_i\rangle}{E_i - E_i^0} \end{aligned} \quad (\text{A4})$$

and

$$\begin{aligned} \langle \psi_m^0 | (H_0 + H') |\psi_i\rangle &= E_i \langle \psi_m^0 | \psi_i\rangle \\ E_m^0 \langle \psi_m^0 | \psi_i\rangle + \langle \psi_m^0 | \hat{H}' | \psi_i\rangle &= E_i \langle \psi_m^0 | \psi_i\rangle \\ \langle \psi_m^0 | \psi_i\rangle &= \frac{\langle \psi_m^0 | \hat{H}' | \psi_i\rangle}{E_i - E_m^0} \quad (m \neq i). \end{aligned} \quad (\text{A5})$$

The procedure is to use the projection operator $1 = \sum_j |\psi_j^0\rangle\langle\psi_j^0|$ progressively with (A4) and (A5) to write the perturbed state wavefunction as a series expansion

$$\begin{aligned} |\psi_i\rangle &= |\psi_i^0\rangle\langle\psi_i^0|\psi_i\rangle + \sum_{m \neq i} |\psi_m^0\rangle\langle\psi_m^0|\psi_i\rangle \\ |\psi_i\rangle &= |\psi_i^0\rangle\langle\psi_i^0|\psi_i\rangle + \sum_{m \neq i} |\psi_m^0\rangle \frac{\langle\psi_m^0|\hat{H}'|\psi_i\rangle}{E_i - E_m^0} \\ |\psi_i\rangle &= |\psi_i^0\rangle\langle\psi_i^0|\psi_i\rangle + \sum_{m \neq i} |\psi_m^0\rangle \left[\frac{\langle\psi_m^0|\hat{H}'|\psi_i^0\rangle}{E_i - E_m^0} \langle\psi_i^0|\psi_i\rangle + \frac{\sum_{l \neq i} \langle\psi_m^0|\hat{H}'|\psi_l^0\rangle\langle\psi_l^0|\psi_i\rangle}{E_i - E_m^0} \right] \end{aligned}$$

$$\begin{aligned}
|\psi_i\rangle &= |\psi_i^0\rangle \langle \psi_i^0 | \psi_i \rangle + \sum_{m \neq i} |\psi_m^0\rangle \frac{\langle \psi_m^0 | H' | \psi_i^0 \rangle}{E_i - E_m^0} \langle \psi_i^0 | \psi_i \rangle + \sum_{\substack{m \neq i \\ \ell \neq i}} |\psi_m^0\rangle \frac{\langle \psi_m^0 | H' | \psi_\ell^0 \rangle}{E_i - E_m^0} \langle \psi_\ell^0 | \psi_i \rangle \\
|\psi_i\rangle &= |\psi_i^0\rangle \langle \psi_i^0 | \psi_i \rangle + \sum_{m \neq i} |\psi_m^0\rangle \frac{\langle \psi_m^0 | H' | \psi_i^0 \rangle}{E_i - E_m^0} \langle \psi_i^0 | \psi_i \rangle + \sum_{\substack{m \neq i \\ \ell \neq i}} |\psi_m^0\rangle \frac{\langle \psi_m^0 | H' | \psi_\ell^0 \rangle}{E_i - E_m^0} \frac{\langle \psi_\ell^0 | H' | \psi_i^0 \rangle}{E_i - E_\ell^0} \langle \psi_i^0 | \psi_i \rangle \\
|\psi_i\rangle &= |\psi_i^0\rangle \langle \psi_i^0 | \psi_i \rangle + \sum_{m \neq i} |\psi_m^0\rangle \frac{\langle \psi_m^0 | H' | \psi_i^0 \rangle}{E_i - E_m^0} \langle \psi_i^0 | \psi_i \rangle + \sum_{\substack{m \neq i \\ \ell \neq i}} |\psi_m^0\rangle \frac{\langle \psi_m^0 | H' | \psi_\ell^0 \rangle}{E_i - E_m^0} \frac{\langle \psi_\ell^0 | H' | \psi_i^0 \rangle}{E_i - E_\ell^0} \langle \psi_i^0 | \psi_i \rangle + \dots \quad (\text{A6})
\end{aligned}$$

Defining $a_i \equiv \langle \psi_i^0 | \psi_i \rangle$ to be the amplitude of the dominant unperturbed ψ_i^0 character in the mixed state ψ_i , we can write this last equation as

$$\begin{aligned}
|\psi_i\rangle &= a_i \left\{ |\psi_i^0\rangle + \sum_{m \neq i} \left[\left(\frac{b_{m,i}}{a_i} \right)_{1\text{st order}} \right. \right. \\
&\quad \left. \left. + \left(\frac{b_{m,i}}{a_i} \right)_{2\text{nd order}} \right] |\psi_m^0\rangle + \dots \right\}, \quad (\text{A7})
\end{aligned}$$

where we identify the first-order and second-order mixing parameters as

$$\left(\frac{b_{m,i}}{a_i} \right)_{1\text{st order}} = \frac{\langle \psi_m^0 | H' | \psi_i^0 \rangle}{E_i - E_m^0} \quad (\text{A8})$$

and

$$\left(\frac{b_{m,i}}{a_i} \right)_{2\text{nd order}} = \sum_{\ell \neq i} \frac{\langle \psi_m^0 | H' | \psi_\ell^0 \rangle \langle \psi_\ell^0 | H' | \psi_i^0 \rangle}{E_i - E_m^0 E_i - E_\ell^0}. \quad (\text{A9})$$

2. Mixing angle, θ , in terms of the perturbed energies

We consider a two-state system and assume that ψ_1^0 and ψ_2^0 are the ‘‘unperturbed’’ eigenfunctions of states 1 and 2, respectively. These eigenfunctions satisfy the time-independent Schrodinger equation

$$\hat{H}^0 \psi_i^0 = E_i^0 \psi_i^0 \quad (i = 1, 2). \quad (\text{A10})$$

We assume that these two states interact via a perturbation term, \hat{H}' , so that the full Hamiltonian is $\hat{H} = \hat{H}^0 + \hat{H}'$. The interaction causes the wavefunctions to mix according to

$$\psi_1 = c_{11} \psi_1^0 + c_{12} \psi_2^0, \quad (\text{A11})$$

$$\psi_2 = c_{21} \psi_1^0 + c_{22} \psi_2^0. \quad (\text{A12})$$

This standard problem in quantum mechanics can be formulated in a matrix representation as

$$\begin{pmatrix} E_1^0 - E_i & H'_{12} \\ H'_{21} & E_2^0 - E_i \end{pmatrix} \begin{pmatrix} c_{i1} \\ c_{i2} \end{pmatrix} = 0. \quad (\text{A13})$$

Solutions are found by setting the determinant of the energy matrix to zero

$$\begin{vmatrix} E_1^0 - E & H'_{12} \\ H'_{21} & E_2^0 - E \end{vmatrix} = 0. \quad (\text{A14})$$

This yields the standard formulas for the energy eigenvalues and eigenfunctions

$$E_{\pm} = \frac{1}{2} (E_2^0 + E_1^0) \pm \frac{1}{2} \sqrt{(E_2^0 - E_1^0)^2 + 4 |H'_{12}|^2}, \quad (\text{A15})$$

$$c_{11} = c_{22} = \frac{|H'_{12}|}{\sqrt{\delta^2 + |H'_{12}|^2}} \equiv \cos \theta, \quad (\text{A16})$$

$$c_{21} = -c_{12} = \frac{\delta}{\sqrt{\delta^2 + |H'_{12}|^2}} \equiv \sin \theta, \quad (\text{A17})$$

where $\delta = (E_+ - E_2^0) = (E_1^0 - E_-)$ is the energy shift (and it is assumed that level 2 lies above level 1). We have also introduced the $\sin \theta$ and $\cos \theta$ notation for the mixing amplitudes because it automatically enforces the orthonormality criteria.

We would like to relate the mixing angle θ to the actual, perturbed (measurable) energies only. To do so, we note that it is straight-forward to show using Eq. (A13) that

$$\Delta \equiv E_2^0 - E_- = E_+ - E_1^0 = \frac{|H'_{12}|^2}{\delta}, \quad (\text{A18})$$

and that the separation of the perturbed energies is $E_+ - E_- = \delta + \Delta$.

From (A16)–(A18), we see

$$\sin \theta \cos \theta (\delta + \Delta) = \frac{\delta |H'_{12}|}{\delta^2 + |H'_{12}|^2} \left(\delta + \frac{|H'_{12}|^2}{\delta} \right) = |H'_{12}|, \quad (\text{A19})$$

and hence,

$$|H'_{12}| = \sin \theta \cos \theta (\delta + \Delta) = \frac{1}{2} \sin 2\theta (E_+ - E_-). \quad (\text{A20})$$

In our case, the two states of interest are the $12(0^+)$ and $11(0^+)$ states, which interact by the spin-orbit term, $H'_{12} = H_{\text{SO}}$, the perturbed energies are the experimentally determined electronic energies, $E_+ = E_{12(0^+)}(R)$ and $E_- = E_{11(0^+)}(R)$, and in principle all quantities can depend on R . Thus

$$|H_{\text{SO}}(R)| = \frac{1}{2} \sin 2\theta(R) [E_{12(0^+)}(R) - E_{11(0^+)}(R)]. \quad (\text{A21})$$

Conversely,

$$\theta(R) = \frac{1}{2} \sin^{-1} \left(\frac{2 |H_{\text{SO}}(R)|}{[E_{12(0^+)}(R) - E_{11(0^+)}(R)]} \right). \quad (\text{A22})$$

- ¹C. Jungen, "Vacuum-ultraviolet emission and absorption spectrum of the NO molecule: The $^2\Delta$ states and their interactions," *Can. J. Phys.* **44**, 3197–3216 (1966).
- ²G. Gouedard and J. C. Lehmann, "Fine-structure determinations in the $x^3\Sigma_g^-$ and $B^3\Sigma_u^-$ states of $^{80}\text{Se}_2$," *J. Phys. B* **9**, 2113–2121 (1976).
- ³R. A. Gottscho, J. B. Koffend, R. W. Field, and J. R. Lombardi, "OODR spectroscopy of BaO. II. New observations of $a^3\Pi$ and $A'^1\Pi$ and re-examination of the Parkinson band system," *J. Chem. Phys.* **68**, 4110–4122 (1978).
- ⁴D. Stahel, M. Leoni, and K. Dressler, "Nonadiabatic representations of the $^1\Sigma_u^+$ and $^1\Pi_u$ states of the N_2 molecule," *J. Chem. Phys.* **79**, 2541–2558 (1983).
- ⁵C. W. Walter, P. C. Cosby, and H. Helm, "Photoexcitation and predissociation intensities of the $c'^1\Sigma_u^+(v=3$ and $4)$, $c^1\Pi_u(v=3$ and $4)$, and $b'^1\Sigma_u^+(v=10, 12, 13,$ and $15)$ states of N_2 ," *J. Chem. Phys.* **112**, 4621–4633 (2000).
- ⁶B. R. Lewis, S. T. Gibson, P. O. O'Keeffe, T. Ridley, K. P. Lawley, and R. J. Donovan, "Observation of completely destructive quantum interference between interacting resonances in molecular photodissociation," *Phys. Rev. Lett.* **86**, 1478–1481 (2001).
- ⁷H. Lefebvre-Brion and R. W. Field, *The Spectra and Dynamics of Diatomic Molecules* (Elsevier, Amsterdam, 2004).
- ⁸A. Shnitman, I. Sofer, I. Golub, A. Yogev, M. Shapiro, Z. Chen, and P. Brumer, "Experimental observation of laser control: Electronic branching in the photodissociation of Na_2 ," *Phys. Rev. Lett.* **76**, 2886–2889 (1996).
- ⁹T. Frohnmeyer and T. Baumert, "Femtosecond pump-probe photoelectron spectroscopy on Na_2 : A tool to study basic coherent control schemes," *Appl. Phys. B* **71**, 259–266 (2000).
- ¹⁰V. S. Batista and P. Brumer, "A direct approach to one photon interference contributions in the coherent control of photodissociation," *J. Chem. Phys.* **114**, 10321–10331 (2001).
- ¹¹B. Li, G. Turinici, V. Ramakrishna, and H. Rabitz, "Optimal dynamic discrimination of similar molecules through quantum learning control," *J. Phys. Chem. B* **106**, 8125–8131 (2002).
- ¹²J. B. Ballard, H. U. Stauffer, E. Mirowski, and S. R. Leone, "Simultaneous control of time-dependent population dynamics and wave-packet quantum interferences in Li_2 by shaped ultrafast pulses," *Phys. Rev. A* **66**, 043402 (2002).
- ¹³M. Shapiro and P. Brumer, "Coherent control of molecular dynamics," *Rep. Prog. Phys.* **66**, 859–942 (2003).
- ¹⁴D. Goswami, "Optical pulse shaping approaches to coherent control," *Phys. Rep.* **374**, 385–481 (2003).
- ¹⁵M. Wollenhaupt, A. Assion, O. Bazhan, C. Horn, D. Liese, C. Sarpe-Tudor, M. Winter, and T. Baumert, "Control of interferences in an Autler-Townes doublet: Symmetry of control parameters," *Phys. Rev. A* **68**, 015401(R) (2003).
- ¹⁶B. H. Hosseini, H. R. Sadeghpour, and N. Balakrishnan, "Control of polarized iodine atom branching ratio in NaI photodissociation," *Phys. Rev. A* **71**, 023402 (2005).
- ¹⁷A. K. Popov, S. A. Myslivets, and T. F. George, "Nonlinear interference effects and all-optical switching in optically dense inhomogeneously broadened media," *Phys. Rev. A* **71**, 043811 (2005).
- ¹⁸K. Ohmori, H. Katsuki, H. Chiba, M. Honda, Y. Hagihara, K. Fujiwara, Y. Sato, and K. Ueda, "Real-time observation of phase-controlled molecular wave-packet interference," *Phys. Rev. Lett.* **96**, 093002 (2006).
- ¹⁹E. H. Ahmed, S. Ingram, T. Kirova, O. Salihoglu, J. Huennekens, J. Qi, Y. Guan, and A. M. Lyyra, "Quantum control of the spin-orbit coupling interaction using the AC Stark effect," *Phys. Rev. Lett.* **107**, 163601 (2011).
- ²⁰E. H. Ahmed, J. Huennekens, T. Kirova, J. Qi, and A. M. Lyyra, "The Autler-Townes effect in molecules: Observations, theory, and applications," in *Advances in Atomic, Molecular, and Optical Physics*, edited by E. Arimondo, P. R. Berman, and C. C. Lin (Elsevier, Amsterdam, 2012), Vol. 61, pp. 467–514.
- ²¹E. H. Ahmed, X. Pan, J. Huennekens, and A. M. Lyyra, "Optical control of collisional population flow between molecular electronic states of different spin multiplicity," *Phys. Rev. A* **89**, 061401(R) (2014).
- ²²S. Eckel, S. Ashman, and J. Huennekens, "Spin-orbit coupling of the NaK $3^3\Pi$ and $3^1\Pi$ states: Determination of the coupling constant and observation of quantum interference effects," *J. Mol. Spectrosc.* **242**, 182–194 (2007).
- ²³F. Masnou-Seeuws and P. Pillet, "Formation of ultracold molecules ($T \leq 200 \mu\text{K}$) via photoassociation in a gas of laser-cooled atoms," *Adv. At., Mol., Opt. Phys.* **47**, 53–127 (2001).
- ²⁴S. Kotochigova, E. Tiesinga, and P. Julienne, "Photoassociative formation of ultracold polar KRb molecules," *Eur. Phys. J. D* **31**, 189–194 (2004).
- ²⁵S. Azizi, M. Aymar, and O. Dulieu, "Prospects for the formation of ultracold ground state polar molecules from mixed alkali atom pairs," *Eur. Phys. J. D* **31**, 195–203 (2004).
- ²⁶A. J. Kerman, J. M. Sage, S. Sainis, T. Bergeman, and D. DeMille, "Production of ultracold, polar RbCs^* molecules via photoassociation," *Phys. Rev. Lett.* **92**, 033004 (2004).
- ²⁷W. C. Stwalley, "Efficient conversion of ultracold Feshbach-resonance-related polar molecules into ultracold ground state ($X^1\Sigma^+ v=0, J=0$) molecules," *Eur. Phys. J. D* **31**, 221–225 (2004).
- ²⁸J. M. Sage, S. Sainis, T. Bergeman, and D. DeMille, "Optical production of ultracold polar molecules," *Phys. Rev. Lett.* **94**, 203001 (2005).
- ²⁹K.-K. Ni, S. Ospelkaus, M. H. G. de Miranda, A. Péer, B. Neyenhuis, J. J. Zirbel, S. Kotochigova, P. Julienne, D. S. Jin, and J. Ye, "A high phase-space-density gas of polar molecules," *Science* **322**, 231–235 (2008).
- ³⁰J. T. Kim, D. Wang, E. E. Eyler, P. L. Gould, and W. C. Stwalley, "Spectroscopy of $^{39}\text{K}^{85}\text{Rb}$ triplet excited states using ultracold $^3\Sigma^+$ state molecules formed by photoassociation," *New J. Phys.* **11**, 055020 (2009).
- ³¹O. Dulieu and C. Gabbanini, "The formation and interactions of cold and ultracold molecules: New challenges for interdisciplinary physics," *Rep. Prog. Phys.* **72**, 086401 (2009).
- ³²S. Ospelkaus, K.-K. Ni, D. Wang, M. H. G. de Miranda, B. Neyenhuis, G. Quémener, P. Julienne, J. L. Bohn, D. S. Jin, and J. Ye, "Quantum-state controlled chemical reactions of ultracold potassium-rubidium molecules," *Science* **327**, 853–857 (2010).
- ³³K. Aikawa, D. Akamatsu, M. Hayashi, K. Oasa, J. Kobayashi, P. Naidon, T. Kishimoto, M. Ueda, and S. Inouye, "Coherent transfer of photoassociated molecules into the rovibrational ground state," *Phys. Rev. Lett.* **105**, 203001 (2010).
- ³⁴N. Bouloufa, M. Pichler, M. Aymar, and O. Dulieu, "Triplet-singlet conversion in ultracold Cs_2 and production of ground-state molecules," *Phys. Rev. A* **83**, 022503 (2011).
- ³⁵P. Zabawa, A. Wakim, A. Neukirch, C. Haimberger, N. P. Bigelow, A. V. Stoliarov, E. A. Pazyuk, M. Tamanis, and R. Ferber, "Near-dissociation photoassociative production of deeply bound NaCs molecules," *Phys. Rev. A* **82**, 040501(R) (2010).
- ³⁶P. Zabawa, A. Wakim, M. Haruza, and N. P. Bigelow, "Formation of ultracold $X^1\Sigma^+(v''=0)$ NaCs molecules via coupled photoassociation channels," *Phys. Rev. A* **84**, 061401(R) (2011).
- ³⁷T. Takekoshi, L. Reichsöllner, A. Schindewolf, J. M. Hutson, C. R. L. Sauer, O. Dulieu, F. Ferlaino, R. Grimm, and H.-C. Nägerl, "Ultracold dense samples of dipolar RbCs molecules in the rovibrational and hyperfine ground state," *Phys. Rev. Lett.* **113**, 205301 (2014).
- ³⁸D. DeMille, "Quantum computation with trapped polar molecules," *Phys. Rev. Lett.* **88**, 067901 (2002).
- ³⁹D. DeMille and E. R. Hudson, "The coldest polar region," *Nat. Phys.* **4**, 911–912 (2008).
- ⁴⁰K. Mishima and K. Yamashita, "Quantum computing using rotational modes of two polar molecules," *Chem. Phys.* **361**, 106–117 (2009).
- ⁴¹L. D. Carr, D. DeMille, R. V. Krems, and J. Ye, "Cold and ultracold molecules: Science, technology and applications," *New J. Phys.* **11**, 055049 (2009).
- ⁴²J. P. Shaffer, W. Chalupczak, and N. P. Bigelow, "Trap loss in a two-species Na-Cs magneto-optical trap: Intramultiplet mixing in heteronuclear ultracold collisions," *Phys. Rev. A* **60**, R3365–R3368 (1999).
- ⁴³C. Haimberger, J. Kleinert, M. Bhattacharya, and N. P. Bigelow, "Formation and detection of ultracold ground-state polar molecules," *Phys. Rev. A* **70**, 021402(R) (2004).
- ⁴⁴O. Docenko, M. Tamanis, J. Zaharova, R. Ferber, A. Pashov, H. Knöckel, and E. Tiemann, "The coupling of the $X^1\Sigma^+$ and $a^3\Sigma^+$ states of the atom pair $\text{Na} + \text{Cs}$ and modelling cold collisions," *J. Phys. B* **39**, S929–S943 (2006).
- ⁴⁵C. Haimberger, J. Kleinert, P. Zabawa, A. Wakim, and N. P. Bigelow, "Formation of ultracold, highly polar $X^1\Sigma^+$ NaCs molecules," *New J. Phys.* **11**, 055042 (2009).
- ⁴⁶A. Grochola, P. Kowalczyk, J. Szczepkowski, W. Jastrzebski, A. Wakim, P. Zabawa, and N. P. Bigelow, "Spin-forbidden $c^3\Sigma^+(\Omega=1) \leftarrow X^1\Sigma^+$ transition in NaCs : Investigation of the $\Omega=1$ state in hot and cold environments," *Phys. Rev. A* **84**, 012507 (2011).
- ⁴⁷A. Wakim, P. Zabawa, M. Haruza, and N. P. Bigelow, "Luminorefrigeration: Vibrational cooling of NaCs ," *Opt. Express* **20**, 16083–16091 (2012).
- ⁴⁸K. Onomichi and H. Katō, "Laser-induced fluorescence of the NaCs molecule," *Bull. Chem. Soc. Jpn.* **56**, 2577–2580 (1983).
- ⁴⁹U. Diemer, H. Weickenmeier, M. Wahl, and W. Demtröder, "Sub-Doppler spectroscopy of the NaCs molecule," *Chem. Phys. Lett.* **104**, 489–495 (1984).

- ⁵⁰O. Docenko, M. Tamanis, R. Ferber, A. Pashov, H. Knöckel, and E. Tiemann, "Spectroscopic studies of NaCs for the ground state asymptote of Na + Cs pairs," *Eur. Phys. J. D* **31**, 205–211 (2004).
- ⁵¹J. Zaharova, M. Tamanis, R. Ferber, A. N. Drozdova, E. A. Pazyuk, and A. V. Stolyarov, "Solution of the fully-mixed state problem: Direct deperturbation analysis of the $A^1\Sigma^+ - b^3\Pi$ complex in a NaCs dimer," *Phys. Rev. A* **79**, 012508 (2009).
- ⁵²S. Ashman, B. McGeehan, C. M. Wolfe, C. Faust, K. Richter, J. Jones, A. P. Hickman, and J. Huennekens, "Experimental studies of the NaCs $5^3\Pi_0$ and $1(a)^3\Sigma^+$ states," *J. Chem. Phys.* **136**, 114313 (2012).
- ⁵³O. Docenko, M. Tamanis, J. Zaharova, R. Ferber, A. Pashov, H. Knöckel, and E. Tiemann, "High resolution spectroscopy and potential determination of the $(3)^1\Pi$ state of NaCs," *J. Chem. Phys.* **124**, 174310 (2006).
- ⁵⁴M. Korek, A. R. Allouche, K. Fakhreddine, and A. Chaalan, "Theoretical study of the electronic structure of LiCs, NaCs, and KCs molecules," *Can. J. Phys.* **78**, 977–988 (2000).
- ⁵⁵M. Korek, S. Bleik, and A. R. Allouche, "Theoretical calculation of the low lying electronic states of the molecule NaCs with spin-orbit effect," *J. Chem. Phys.* **126**, 124313 (2007).
- ⁵⁶M. Aymar and O. Dulieu, "Calculations of transition and permanent dipole moments of heteronuclear alkali dimers NaK, NaRb and NaCs," *Mol. Phys.* **105**, 1733–1742 (2007).
- ⁵⁷B. A. Palmer, R. A. Keller, and R. Engleman, "An atlas of Uranium emission intensities in a hollow cathode discharge," LASL Report No. LA-8251-MS, 1980.
- ⁵⁸S. Gerstenkorn and P. Luc, *Atlas du Spectre D'absorption de la Molécule D'Iode* (Centre National de la Recherche Scientifique, Paris, 1978).
- ⁵⁹R. Stair, W. E. Schneider, and J. K. Jackson, "A new standard of spectral irradiance," *Appl. Opt.* **2**, 1151–1154 (1963).
- ⁶⁰J. A. Jones, "Studies of inelastic collisions of NaK and NaCs molecules with atomic perturbers," Ph.D. dissertation (Lehigh University, 2015).
- ⁶¹J. Huennekens, I. Prodan, A. Marks, L. Sibbach, E. Galle, T. Morgus, and L. Li, "Experimental studies of the NaK $1^3\Delta$ state," *J. Chem. Phys.* **113**, 7384–7397 (2000).
- ⁶²P. Burns, L. Sibbach-Morgus, A. D. Wilkins, F. Halpern, L. Clarke, R. D. Miles, L. Li, A. P. Hickman, and J. Huennekens, "The $4^3\Sigma^+$ state of NaK: Potential energy curve and hyperfine structure" *J. Chem. Phys.* **119**, 4743–4754 (2003).
- ⁶³L. Morgus, P. Burns, R. D. Miles, A. D. Wilkins, U. Ogba, A. P. Hickman, and J. Huennekens, "Experimental study of the NaK $3^3\Pi$ double minimum state," *J. Chem. Phys.* **122**, 144313 (2005).
- ⁶⁴A. D. Wilkins, L. Morgus, J. Hernandez-Guzman, J. Huennekens, and A. P. Hickman, "The NaK $1^{1,3}\Delta$ states: Theoretical and experimental studies of fine and hyperfine structure of rotational levels near the dissociation limit," *J. Chem. Phys.* **123**, 124306 (2005).
- ⁶⁵R. D. Miles, L. Morgus, D. O. Kashinski, J. Huennekens, and A. P. Hickman, "Nonadiabatic coupling in the $3^3\Pi$ and $4^3\Pi$ states of NaK," *J. Chem. Phys.* **125**, 154304 (2006).
- ⁶⁶L. Li and R. W. Field, "Direct observation of high-lying $^3\Pi_g$ states of the Na₂ molecule by optical-optical double resonance," *J. Phys. Chem.* **87**, 3020–3022 (1983).
- ⁶⁷R. J. Le Roy, DParFit 3.3: A computer program for fitting diatomic molecule spectral data to parameterized level energy expressions, University of Waterloo, 2005, can be downloaded from the website <http://leroy.uwaterloo.ca/programs/>.
- ⁶⁸R. Rydberg, "Graphische darstellung einiger bandenspektroskopischer ergebnisse," *Z. Phys.* **73**, 376–385 (1931).
- ⁶⁹O. Klein, "Zur berechnung von potentialkurven für zweiatomige moleküle mit hilfe von spektraltermen," *Z. Phys.* **76**, 226–235 (1932).
- ⁷⁰A. L. G. Rees, "The calculation of potential-energy curves from band-spectroscopic data," *Proc. Phys. Soc.* **A59**, 998–1008 (1947).
- ⁷¹R. J. Le Roy, RKR1 2.0: A computer program implementing the first-order RKR method for determining diatomic molecule potential energy functions, University of Waterloo, 2004, can be downloaded from the website <http://leroy.uwaterloo.ca/programs/>.
- ⁷²R. J. Le Roy, Level 8.0: A computer program for solving the radial Schrödinger equation for bound and quasibound levels, University of Waterloo, 2007, can be downloaded from the website <http://leroy.uwaterloo.ca/programs/>.
- ⁷³C. Vidal and H. Scheingraber, "Determination of diatomic molecular constants using an inverted perturbation approach: Application to the $A^1\Sigma_u^+ - X^1\Sigma_g^+$ system of Mg₂," *J. Mol. Spectrosc.* **65**, 46–64 (1977).
- ⁷⁴A. Pashov, W. Jastrzębski, and P. Kowalczyk, "Construction of potential curves for diatomic molecular states by the IPA method," *Comput. Phys. Commun.* **128**, 622–634 (2000).
- ⁷⁵R. J. Le Roy and G. T. Kraemer, Bcont 2.2: A computer program for calculating bound \rightarrow continuum transition intensities for diatomic molecules, University of Waterloo, 2004, can be downloaded from the website <http://leroy.uwaterloo.ca/programs/>.
- ⁷⁶B. M. McGeehan, S. Ashman, C. M. Wolfe, R. Steinhardt, M. L. Monaco, J. Huennekens, and A. P. Hickman, "NaK bound-free and bound-bound $4^3\Sigma^+ \rightarrow a^3\Sigma^+$ emission," *J. Mol. Spectrosc.* **265**, 74–80 (2011).
- ⁷⁷B. McGeehan, "Investigation of bound-free emission spectra of NaK," Ph.D. dissertation (Lehigh University, 2010).
- ⁷⁸C. E. Faust, "Experimental studies of interacting electronic states in NaCs," Ph.D. dissertation (Lehigh University, 2014).
- ⁷⁹H. Salami, T. Bergeman, B. Beser, J. Bai, E. Ahmed, S. Kotochigova, A. M. Lyyra, J. Huennekens, C. Lisdat, A. V. Stolyarov, O. Dulieu, P. Crozet, and A. J. Ross, "Spectroscopic observations, spin-orbit functions, and coupled channels deperturbation analysis of data on the $A^1\Sigma_u^+$ and $b^3\Pi_u$ states of Rb₂," *Phys. Rev. A* **80**, 022515 (2009).
- ⁸⁰H. Harker, P. Crozet, A. J. Ross, K. Richter, J. Jones, C. Faust, J. Huennekens, A. V. Stolyarov, H. Salami, and T. Bergeman, "Experimental and theoretical studies of the coupled $A^1\Sigma^+$ and $b^3\Pi$ states of NaK," *Phys. Rev. A* **92**, 012506 (2015).